

# 1D Edge Contacts to 2D Material Heterostructures

Master's Thesis in Erasmus Mundus Master of Science in Nanoscience and Nanotechnology (Nanoelectronics)

**BOGDAN KARPIAK**



MASTER'S THESIS IN ERASMUS MUNDUS MASTER OF SCIENCE  
IN NANOSCIENCE AND NANOTECHNOLOGY

# 1D Edge Contacts to 2D Material Heterostructures

BOGDAN KARPIAK



**CHALMERS**  
UNIVERSITY OF TECHNOLOGY

Department of Microtechnology and Nanoscience (MC2)  
*Quantum Device Physics*  
CHALMERS UNIVERSITY OF TECHNOLOGY  
Gothenburg, Sweden 2016

1D Edge Contacts to 2D Material Heterostructures  
BOGDAN KARPIAK

© BOGDAN KARPIAK, 2016.

Supervisor: Assoc. Prof. Saroj Prasad Dash, Chalmers University of Technology

Co-Promoter: Prof. Bart Sorée, KU Leuven

Examiner: Dr. Huan Zhao Ternehäll, Chalmers University of Technology

Master's Thesis in Erasmus Mundus Master of Science in Nanoscience and  
Nanotechnology

Department of Microtechnology and Nanoscience (MC2)

Quantum Device Physics

Chalmers University of Technology

SE-412 96 Gothenburg

Telephone +46 31 772 1000

Cover: Optical image of one of the batch-fabricated Hall elements along with the schematics of one-dimensional edge contact to h-BN encapsulated graphene sheet with grey spheres representing carbon atoms in graphene sheet as well as orange and green spheres representing nitrogen and boron atoms respectively in a h-BN crystal. Transport of free electrons from the contact lead into the graphene sheet is also shown in the schematics.

Typeset in L<sup>A</sup>T<sub>E</sub>X

Printed by Chalmers Reproservice

Gothenburg, Sweden 2016

1D Edge Contacts to 2D Material Heterostructures  
Master's Thesis in Erasmus Mundus Master of Science in Nanoscience and Nanotechnology  
BOGDAN KARPIAK  
Department of Microtechnology and Nanoscience  
Quantum Device Physics  
Chalmers University of Technology

## Abstract

Graphene has been in the focus of research in many fields of applications due to its unique properties. In particular, the 2D nature, low charge carrier concentration and high mobility of carriers are promising properties for the use in magnetic Hall sensors. At the same time, low spin-orbit coupling and negligible hyperfine interactions make it interesting for spin-polarized electron transport. However, single graphene layer, if unprotected, is prone to defects introduced during fabrication processes and also defects due to interfaces with other insulators or contact materials. These factors would inevitably lead to decrease of graphene device performance. By encapsulating graphene in hexagonal boron nitride (h-BN), another insulating atomically flat two-dimensional (2D) material with superior interface properties with graphene, one can fabricate heterostructures for robust and high-performance devices. Utilizing one-dimensional (1D) edge contacts to graphene sheet in such devices based on 2D materials would also allow to minimize contacts-induced degradation of channel properties.

The graphene/h-BN heterostructures for studied devices were prepared both by exfoliation from bulk crystals and by transfer of CVD-grown materials over large area. After patterning the 2D heterostructures, 1D edge contacts were fabricated by means of electron or laser beam lithography and electron beam evaporation of metals. In these devices, proof-of-concept for batch fabrication of Hall elements on large area all-CVD h-BN/graphene/h-BN heterostructures is demonstrated. Such 1D edge contacts of ferromagnetic materials to graphene/h-BN heterostructures are also explored for spin injection into graphene in devices with novel design.

The findings described in this thesis allow to advance the graphene Hall elements fabrication technology towards large-scale, industry-compatible manufacturing and lay basis for understanding and further optimization of the phenomena that drive and influence the operation of graphene spin-based devices with novel design involving 1D edge contacts.

Keywords: graphene, hexagonal boron nitride, 2D materials, van der Waals heterostructures, 1D edge contacts, Hall sensors, nonlocal spin valve, local Hall effect.



## To be published

Based on the findings described in this thesis the following manuscripts are to be submitted for publication:

- I. Novel graphene spin valve device with 1D edge contacts and influence of local Hall effect.**  
B. Karpiak, A. Dankert, S.P. Dash.
- II. Gate-tunable magnetic Hall sensors on large area CVD graphene protected by exfoliated h-BN and with 1D edge contacts.**  
B. Karpiak, A. Dankert, S.P. Dash.
- III. Magnetic Hall sensors batch-fabricated on all-CVD graphene/h-BN heterostructures with 1D edge contacts.**  
B. Karpiak, A. Dankert, S.P. Dash.



## Acknowledgements

First and foremost, I would like to express my gratitude to Professor Saroj P. Dash. I would like to thank him for the opportunity to do this master thesis in his research team on the topic that I found to be very interesting. His constant guidance, openness to suggestions and discussions made this experience truly enriching.

My gratitude goes to André. Discussions with him and especially assistance in practical matters were very helpful.

Thank you Priya for creating the smooth start at the beginning of this project and assistance in practical matters.

Thanks to MC2 department and QDP in particular for the comfortable working environment.

I would like to acknowledge also the European Commission for creating such financial opportunities for foreign students to obtain high-quality education in among the best universities in Europe.

And my sincere gratitude goes to my parents who were always there to support me in any critical situation.

Bogdan Karpiak, Gothenburg, July 2016



## List of abbreviations

1D	One-dimensional
2D	Two-dimensional
h-BN	Hexagonal boron nitride
CVD	Chemical vapour deposition
FM	Ferromagnetic
EBL	Electron beam lithography
AFM	Atomic force microscopy
IV	Current-voltage
PMMA	Poly(methyl methacrylate)
IPA	Isopropyl alcohol



# Contents

<b>To be published</b>	<b>vii</b>
<b>Acknowledgements</b>	<b>ix</b>
<b>List of abbreviations</b>	<b>xi</b>
<b>List of Figures</b>	<b>xv</b>
<b>1 Introduction</b>	<b>1</b>
<b>2 Fabrication</b>	<b>3</b>
2.1 Lithography . . . . .	3
2.1.1 Electron beam lithography . . . . .	4
2.1.2 Laser beam lithography . . . . .	4
2.2 Surface preparation, deposition of metals and heterostructures etching	4
2.2.1 Annealing . . . . .	4
2.2.2 Electron beam evaporations of metals . . . . .	5
2.2.3 Reactive ion etching . . . . .	5
2.3 Processes . . . . .	5
2.3.1 Chip preparation . . . . .	5
2.3.2 Two-dimensional layered van der Waals heterostructures . . . . .	5
2.3.2.1 Exfoliation from bulk crystals . . . . .	5
2.3.2.2 Transfer of CVD-grown materials . . . . .	6
2.3.2.3 2D heterostructures patterning . . . . .	6
2.4 Device fabrication . . . . .	7
2.4.1 Devices fabricated on CVD graphene/exfoliated h-BN heterostructures . . . . .	7
2.4.2 Batch-fabricated Hall elements on heterostructures of all-CVD h-BN/graphene/h-BN . . . . .	8
<b>3 Novel graphene spin valve device and influence of local Hall effect</b>	<b>9</b>
3.1 Introduction . . . . .	9
3.2 Results and discussion . . . . .	11
3.3 Conclusions . . . . .	17
<b>4 Graphene-based magnetic Hall sensors protected by exfoliated h-BN</b>	<b>19</b>
4.1 Introduction . . . . .	19

4.2	Results and discussion . . . . .	21
4.3	Conclusions . . . . .	25
<b>5</b>	<b>Magnetic Hall sensors based on all-CVD 2D materials</b>	<b>27</b>
5.1	Introduction . . . . .	27
5.2	Results and discussion . . . . .	28
5.3	Conclusions . . . . .	32
<b>6</b>	<b>Conclusions</b>	<b>35</b>
	<b>Appendix A</b>	<b>37</b>
	<b>Appendix B</b>	<b>39</b>
	<b>Bibliography</b>	<b>41</b>

# List of Figures

2.1	Lithography processing steps with two layers of resists for improved liftoff . . . . .	4
2.2	Processing steps of CVD graphene transfer . . . . .	6
2.3	Fabrication of devices comprising of heterostructures of CVD graphene and exfoliated h-BN . . . . .	7
2.4	Optical micrographs of batch-fabricated Hall elements comprising of all-CVD h-BN/graphene/h-BN heterostructures . . . . .	8
3.1	Conventional approach for spin injection/detection in graphene with surface top ferromagnetic contacts . . . . .	10
3.2	Novel nonlocal spin valve device concept with 1D edge ferromagnetic contacts to graphene . . . . .	11
3.3	Fabrication of novel nonlocal spin valve device with 1D edge ferromagnetic (TiO <sub>2</sub> /Co) contacts to graphene/h-BN heterostructure . . .	12
3.4	Characterization of graphene/h-BN heterostructures in novel nonlocal spin valve device with 1D edge contacts . . . . .	12
3.5	Magnetoresistance measurements of the spin valve device and bias dependence . . . . .	13
3.6	Temperature dependence of magnetoresistance signal in novel nonlocal spin valve device . . . . .	15
3.7	Gate dependence of magnetoresistance signal in novel nonlocal spin valve device . . . . .	16
4.1	An overview of the field of magnetic sensors and their applications with corresponding detectable magnetic field ranges. . . . .	20
4.2	Fabrication of CVD graphene/exfoliated h-BN heterostructures with 1D edge contacts: schematics, optical microscopy picture and fabrication process steps . . . . .	21
4.3	Characterization of CVD graphene/exfoliated h-BN heterostructures and 1D edge contacts: Raman spectrum and typical 2-terminal IV characteristic . . . . .	22
4.4	Operation of CVD graphene/exfoliated h-BN Hall elements: perpendicular magnetic field and time dependencies of Hall voltage, current bias dependence of current-related sensitivity. . . . .	23
4.5	Gate tunability of operation of CVD graphene/exfoliated h-BN Hall sensors . . . . .	24

5.1	Fabrication of magnetic Hall elements based on large area CVD graphene encapsulated in h-BN on Si/SiO <sub>2</sub> substrate: schematics, optical microscopy picture and fabrication process steps . . . . .	28
5.2	Characterization of the heterostructures and 1D contacts in graphene Hall elements based on only CVD materials . . . . .	29
5.3	Graphene channel characterization in Hall sensors based on all-CVD materials . . . . .	29
5.4	The distribution of sheet resistance and Hall mobility of h-BN-encapsulated graphene within a batch of 13 graphene Hall elements . . . . .	30
5.5	Characterization of operation of all-CVD based graphene Hall elements at two different temperatures . . . . .	31
5.6	Current-related sensitivities of graphene Hall elements: temperature dependence, current bias dependence and histogram of distribution within a batch of 13 graphene Hall elements . . . . .	31
A.1	Operation of graphene Hall sensors with exfoliated h-BN protection at low temperature . . . . .	37

# Chapter 1

## Introduction

The proper choice of functional materials in any technology is a key to its successful development. While Si is highly common material in today's electronic devices and Si-based technology is highly mature, other materials such as III-V compound semiconductors are also considered. New functional materials with the required properties are necessary to solve the increasing challenges posed by the trend of shrinking logic and memory device dimensions for improved performances, less energy consumption and decreased cost per functionality [1].

Inspired by the discovery of graphene [2], the field of 2D van der Waals heterostructures [3–5] has emerged and been extensively studied [6,7]. The 2D materials possess unique properties which have focused significant amount of research efforts towards implementation of new generation of devices based on the heterostructures of atomically thin layered materials. By assembling such layers of distinct 2D materials, held together by the weak van der Waals forces, one could potentially tune the required functionality and combined properties of the assembled structures. Moreover, such heterostructures, instead of simply replacing the old materials for improved functionality within the frame of the same working principles, could be utilized to invent novel devices that operate based on fundamentally different properties such as spins.

The graphene is among the most promising candidates to be used in such heterostructures due to its excellent properties. Having purely 2D nature and consisting of only one layer of carbon atoms arranged in sheets of honeycomb lattice, this material is mechanically extremely strong in atomic scale due to the in-plane  $\sigma$ -bonds between carbon atoms, while the completely delocalized electrons in the  $\pi$ -bonds give rise to excellent charge conductivity and high mobility [8]. The peculiar zero-gap band structure with linear energy dispersion near the charge neutrality (Dirac) point in this semimetallic, Dirac material [9,10] allow to tune the charge concentration as well as the type of charge carriers (holes or electrons) by means of electrical fields [2]. These properties, among others, make graphene highly appealing for a variety of applications [6,7] and, in particular, in spintronics and Hall sensors.

Spintronics introduces a new paradigm in operation of electronic devices and could potentially give rise to new generation of non-volatile logic and memory circuitry that could operate with less power consumption [11]. Information in such devices is encoded in the orientation of electrons' spins, which could be injected by electrical means from ferromagnetic metals into spin transport channel for further

manipulation and detection. Graphene, due to its intrinsic low spin-orbit coupling and negligible hyperfine interactions [7, 12, 13], is a promising material for utilization as a spin transport channel for transmission of spin-based information over relatively long distances [14].

The field of Hall elements, another interesting direction for application of graphene [15–20], today covers a wide range of sensors that are based on Hall effect [21–23]. Such sensors are used in medical, consumer, industrial, automotive segments, among others, and constitute a significant growing market [24, 25]. Fostered by the constant strive for performance improvements and market price reduction, new materials are being considered for utilization in active regions of Hall sensors to replace the III-V compound semiconductors [26–28] and more traditional Si [22, 23, 29, 30]. The 2D nature, low carrier concentration and high mobility make graphene highly promising for utilization in active regions of Hall sensors.

However, the one-layer-thick graphene is sensitive to environmental influences which have negative impact on material characteristics. To reduce degradation of the intrinsic graphene properties for reliable device performances, a proper insulating material with good interface qualities to graphene has to be used. For this purpose heterostructures of graphene and hexagonal boron nitride (h-BN) can be utilized. The latter is a wide bandgap ( $\sim 6$  eV) insulator [31] with honeycomb lattice having little mismatch ( $\sim 1.7$  %) with graphene [32]. The interface between atomically flat h-BN and graphene contains low amount of dangling bonds and charge traps [33], making it an appealing material for graphene protection from the environmental influences.

The customary approach for contacting graphene active regions utilizes fabrication of contacts on the surface of graphene. However, this creates certain limitations and challenges that reduce application potential of devices involving heterostructures of graphene and h-BN. Thus, surface contacts can introduce additional spin dephasing in the transport channel underneath them [34, 35] and cause doping of graphene [36, 37], which is especially detrimental for Hall sensor applications [15]. Furthermore, large-scale fabrication of graphene devices with h-BN protection is limited due to the necessity to expose the unprotected graphene regions for deposition of contact materials [38]. These problems can be significantly reduced by contacting the graphene sheet from the edge forming the 1D edge contacts to carbon atoms [38].

In this thesis heterostructures of graphene and h-BN with 1D edge contacts are investigated for their utilization in spintronic devices and Hall sensors. Chapter 2 briefly introduces the reader to main techniques and processes used during the fabrication of investigated samples. While Chapter 3 focuses on the findings revealed in samples aimed at study of graphene spin transport properties in novel device design, Chapters 4 and 5 are dedicated to investigation of Hall sensors with active regions comprised of CVD graphene/exfoliated h-BN and all-CVD h-BN/graphene/h-BN heterostructures respectively.

For more elaborate, application-specific introductions to the role of heterostructures of graphene and h-BN with 1D edge contacts in spin-based devices and Hall sensors the reader is referred to Sections 3.1, 4.1 and 5.1.

## Chapter 2

### Fabrication

The fabrication of micro- and nanodevices, especially those that are based on ultra-thin two-dimensional materials, requires special environmental conditions and tools. All of the devices presented in this thesis were fabricated in MC2 Nanofabrication Laboratory at Chalmers University of Technology. This chapter describes the techniques and processes used. For detailed step-by-step recipes the reader is referred to Appendix B.

#### 2.1 Lithography

Lithography process steps constitute an essential part in fabrication of micro- and nanodevices since they provide means for patterning the functional materials. Among the popular lithographic techniques photolithography and electron beam lithography can be distinguished based on the source of exposure. While each technique has both advantages and drawbacks, they consist of essentially similar processing steps.

First, the chip is covered with a polymer resist by spinning the wafer with the polymer on top. This allows for more homogeneous resist coverage over the wafer surface with more uniform resist thicknesses in the central regions of the wafer. After spinning the chip is baked to evaporate the solvents. During the following exposure step by the corresponding source the exposed resist regions undergo chemical reactions which change their local solubility, making them sensitive or robust (depending on whether the resist is positive or negative respectively) to development in special chemicals. The exposure mask, which defines which regions are to be exposed, can be a separate layer of opaque material put between the light source and the resist layer as it usually is in case of photolithography. In case of laser and electron beam lithography, the mask defines the paths which the laser or electron beam respectively have to follow during the exposure process and it is prepared by means of computer software programs such as AutoCAD. Thus, after the exposure and development steps, the intricate patterns of resist mask can be formed with designed regions open for deposition of new materials or etching of underlying ones. After the deposition step during the liftoff in order to allow the solvents such as acetone to reach the underlying resist mask and remove it along with the superfluous materials deposited on top of it, the resist mask has to be thicker than the combined thickness of deposited materials. To further ensure the successful liftoff process, bilayer resist mask is used for electron beam lithography (Figure 2.1). This allows for relatively wider opening on the bottom resist layer for better access of solvents.

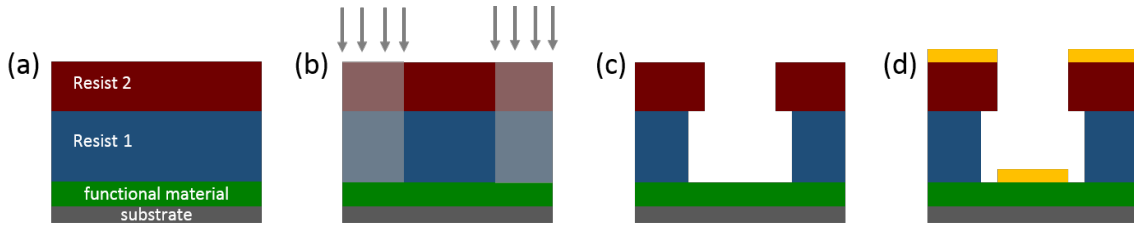


**Figure 2.1:** Lithography processing steps with two layers of resists for improved liftoff. Negative resists are considered. (a) Spin-coating the wafer containing functional materials that are to be patterned with 2 layers of resists. (b) Exposing the resist regions that are to form the mask pattern. (c) After the development of unexposed regions and (d) evaporations of metals (yellow). After the liftoff, the resists with evaporated metals on top are removed leaving only the metals in the openings.

### 2.1.1 Electron beam lithography

This is specialized lithography technique that is mostly used in research applications. The technique utilizes a scanning beam of high-energy electrons, which expose the regions of resists defined by a mask created by means of computer software such as AutoCAD. It is slow if to compare to optical lithography, but provides flexibility for creating intricate patterns without the need in very expensive hard masks for each new pattern. Additionally, the electron beam lithography is capable of very high resolutions for creating extremely fine patterns ( $\sim 50 \text{ nm}$ ). However, the tool itself is complicated and can be very expensive [39].

### 2.1.2 Laser beam lithography

Similarly to electron beam lithography, this technique utilizes a scanning laser beam on the surface of resists to form a pattern. It is flexible technique and does not require a hard mask. However, laser beam lithography provides faster exposure rates while the resolution is limited to  $\sim 1 \mu\text{m}$  depending on the mode used.

## 2.2 Surface preparation, deposition of metals and heterostructures etching

### 2.2.1 Annealing

Graphene is known for its unique intrinsic properties and, in particular, ultra-high mobilities. But as soon as it is brought in contact with other materials, these properties can deteriorate drastically. While some materials, such as hexagonal boron nitride, induce less negative influence on graphene [33], the residues of e.g. resists or other adatoms are always present to some extent at the interface causing additional negative impact on graphene properties. Additionally, in some applications the interface itself between graphene and e.g. ferromagnetic contacts play a crucial role. Thus, there is a necessity in formation of high-quality, clean and residue-free

graphene surface. For this purpose annealing can be utilized since it facilitates decomposition and removal of residues [40]. The annealing of graphene devices is usually performed in Ar/H<sub>2</sub> atmosphere. This processing step is also sometimes performed as the last step of device fabrication to reduce resistances of contacts.

### 2.2.2 Electron beam evaporations of metals

This technique is a form of physical vapour deposition. It utilizes a high-energy focused by magnetic field beam of electrons emitted from a tungsten filament. Upon slowing down in the material that is to be evaporated, the electrons heat it up so that it melts and vapours of this material are formed. Upon reaching the substrate, these vapours condense and form a thin layer of deposited material. The whole process undergoes in high vacuum conditions of  $\sim 5 \times 10^{-7}$  Torr to reduce contaminations.

### 2.2.3 Reactive ion etching

This is a type of dry etching. This technique utilizes chemically reactive ion plasma which can be used for resist striping or etching of functional materials. Thus, oxygen plasma is used for graphene etching, but it cannot be utilized for removal of hexagonal boron nitride. For this purpose a plasma consisting of a mixture of O<sub>2</sub> and CHF<sub>3</sub> is used, which can remove both the graphene and h-BN.

## 2.3 Processes

### 2.3.1 Chip preparation

As a chip substrate heavily-doped Si  $7 \times 7$  mm covered with  $\sim 285$  nm of SiO<sub>2</sub> is used. The chosen silicon oxide thickness ensures good optical contrast of graphene. The gold markers are prefabricated on the surface for easy locating.

### 2.3.2 Two-dimensional layered van der Waals heterostructures

There are two ways of producing two-dimensional materials: exfoliation and chemical vapour deposition (CVD) growth. The first method is widely used in research purposes and provides materials of good quality, but it lacks scalability which is necessary for industrial applications. The CVD growth, on the contrary, is a promising scalable technique. It utilizes growth on catalytic substrates such as copper and produces thin layers of two-dimensional materials, which afterwards can be transferred on the desirable substrate for further processing and device fabrication.

#### 2.3.2.1 Exfoliation from bulk crystals

The devices investigated in this thesis utilized the exfoliation method only for producing the flakes of hexagonal boron nitride (h-BN). The regular scotch tape method was exploited for exfoliation.

First, the thick flake of h-BN was cleaved from bulk crystal using the tape of low adhesiveness. Such cleavage is possible due to the weak van der Waals adhesion force between different layers of h-BN. Next, by means of multiple exfoliations from the tape, the flakes are scattered with decreasing thicknesses. Finally, by applying a slight pressure, the scattered flakes are transferred onto the desired substrate. Such steps result in a number of flakes of different shapes and dimensions. They are inspected by means of optical microscope and the most appropriate ones are located for device fabrication. Typical thickness of exfoliated flakes of h-BN  $\sim 25$  nm.

### 2.3.2.2 Transfer of CVD-grown materials

The CVD graphene and h-BN, used for device fabrication, were obtained from Graphenea [41] and Graphene Supermarket [42] respectively. Since the CVD growth is performed on special substrates (e.g. copper) which catalyze the growth process, afterwards the two-dimensional materials have to be transferred on the desired insulating substrate for further device fabrication. The wafer scale transfer of CVD materials for devices used in this thesis is service of Graphenea.

Schematically the processing steps of CVD graphene transfer are provided in Figure 2.2. First, the graphene on one side of copper substrate is removed by means of thermal release tape followed by the transfer of the remaining graphene on the other side of copper foil onto the desired substrate using PMMA sacrificial layer.

### 2.3.2.3 2D heterostructures patterning

In order to fabricate devices of desired dimensions and shapes of active regions patterning is essential. For this purpose either electron beam lithography or laser beam lithography was utilized (see Section 2.1). This allowed to create resist masks

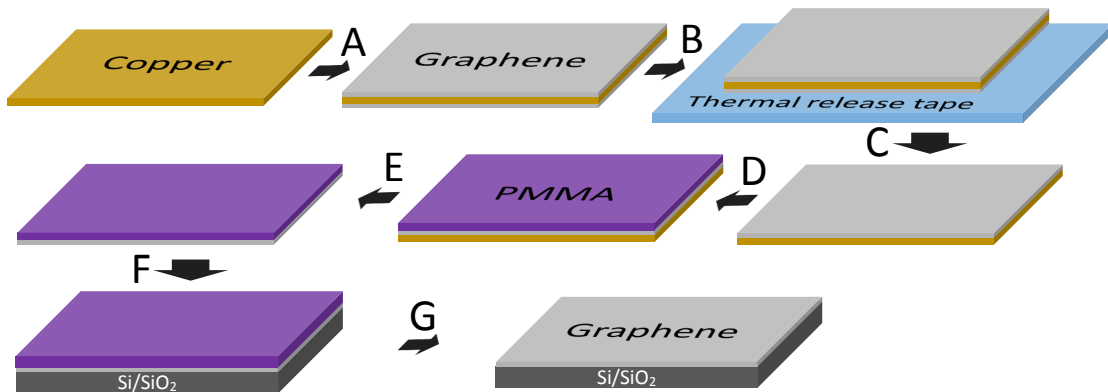


**Figure 2.2:** Processing steps of CVD graphene transfer according to [43]. First, the graphene grows on copper foil on both sides (A). Next, thermal release adhesive tape is put onto the graphene surface (B) followed by its removal along with the graphene on one side of copper foil after heating (C). After covering the graphene with sacrificial protective layer (PMMA) (D), copper is etched away in  $\text{FeCl}_3$  (E) and graphene is mechanically transferred onto the  $\text{Si/SiO}_2$  substrate (F). Finally, the sacrificial layer is dissolved (G).

for removal of any excessive regions of graphene/h-BN heterostructures that are not used in the active regions of the fabricated devices. The materials were etched by means of reactive ion etching (see Subsection 2.2.3).

## 2.4 Device fabrication

This section describes the processing steps used for fabrication of devices studied in this thesis. In particular, the fabrication of devices investigated in Chapters 3 and 4 is described in Subsection 2.4.1, whereas fabrication of devices investigated in Chapter 5 is described in Subsection 2.4.2.

### 2.4.1 Devices fabricated on CVD graphene/exfoliated h-BN heterostructures

The heterostructures were prepared by first transferring the large area CVD graphene from copper foil onto Si/SiO<sub>2</sub> substrate (service of Graphenea, see Subsection 2.3.2.2). After cleaning the surface of graphene from resist residues first in warm acetone and afterwards by annealing in Ar/H<sub>2</sub> atmosphere (see Subsection 2.2.1), the h-BN was exfoliated (see Subsection 2.3.2.1) on top (Figure 2.3a). Finally, the superfluous graphene, not covered by h-BN, was removed by oxygen plasma etching (Subsection 2.2.3) leaving only the regions with graphene/h-BN heterostructures on the Si/SiO<sub>2</sub> substrate. The electron beam lithography (Subsection 2.1.1) processing steps (using the exposure pattern designed in AutoCAD) were utilized for fabrication of ferromagnetic contacts (1 nm TiO<sub>2</sub>/65 nm Co), which were deposited by electron beam evaporation of metals (Subsection 2.2.2). To form the tunnel barrier of  $\sim 1$  nm TiO<sub>2</sub>, the procedure of deposition of thin film of Ti ( $\sim 0.4$  nm) and its oxidation in pure oxygen atmosphere under 10 Torr pressure for 10 minutes was repeated twice. The fabricated device is shown in Figure 2.3b.

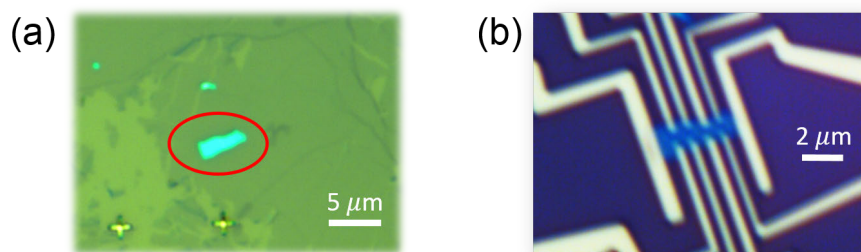


**Figure 2.3:** Fabrication of devices comprising of heterostructures of CVD graphene and exfoliated h-BN. (a) Optical microscopy picture with highlighted region showing one of the selected h-BN flakes after exfoliation on large area CVD graphene and (b) optical image of the fabricated device with ferromagnetic contacts.

### 2.4.2 Batch-fabricated Hall elements on heterostructures of all-CVD h-BN/graphene/h-BN

For preparation of all-CVD h-BN/graphene/h-BN heterostructures, the corresponding CVD materials were successively transferred onto Si/SiO<sub>2</sub> substrate forming the heterostructures over large area (service of Graphenea). To pattern the heterostructures for device fabrication, laser beam lithography (Subsection 2.1.2) was utilized. This allowed to form a 20 nm-thick Al hard mask for etching the superfluous heterostructure regions with CHF<sub>3</sub>/O<sub>2</sub> plasma (Subsection 2.2.3). Next, the Al hard mask was etched away by MF319 followed by annealing and another series of laser beam lithography processing steps for fabrication of contacts by electron beam evaporations of metals (20 nm Ti/60 nm Au). The optical microscopy pictures of the Hall elements batch-fabricated on large area all-CVD h-BN-encapsulated graphene are provided in Figure 2.4.

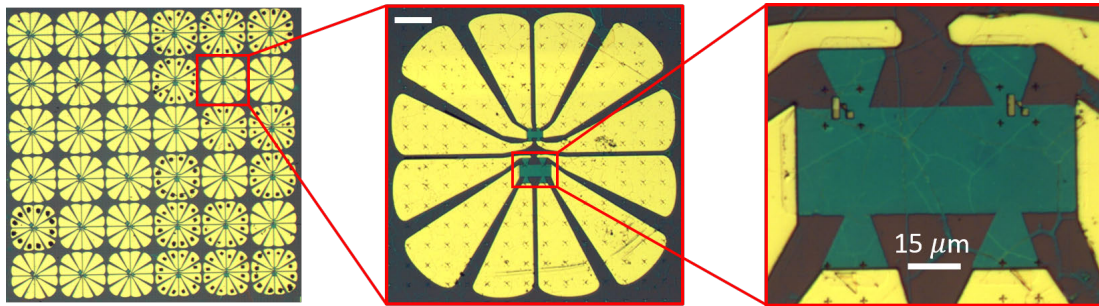


**Figure 2.4:** Optical micrograph of an array of batch-fabricated Hall elements on all-CVD h-BN/graphene/h-BN heterostructures ( $4.5 \times 4.5$  mm, left) and enlarged regions of two Hall elements of different size with 6 contact pads for each of them (middle image, scale bar at the top left corresponds to  $100 \mu\text{m}$ ) and closer look at one of the fabricated Hall elements (right).

## Chapter 3

### Novel graphene spin valve device with 1D edge contacts and influence of local Hall effect

Graphene is known as an effective spin transport medium owing to its low spin-orbit coupling and negligible hyperfine interactions. The conventional spin valve devices for the study of spin communication in graphene utilize metallization of its surface for fabrication of contacts which include tunnel barrier essential for improved spin injection. However, such tunnel barriers usually suffer from pin-holes, surface roughness and other defects which contribute to additional spin dephasing at the graphene/contacts interfaces. This chapter investigates the novel nonlocal spin valve devices with CVD graphene/h-BN heterostructures and 1D edge contacts, which are expected to reduce the contact area as well as the mentioned interface problems related to it. The nonlocal spin valve measurements demonstrate extraneous magnetoresistance switching behaviour which is shown to be dominated by the local Hall effect in the presence of fringe fields from ferromagnetic contacts, which have more prominent influence on device operation in edge contact geometry. Systematic measurements of the signal were carried out at different current biases, temperatures and gate voltages. Only one switching of the magnetoresistance signal was observed supporting the argument in favor of the nature of observed behaviour due to local Hall effect as well as the gate voltage dependence of nonlocal device response, where a change of sign of the signal is observed on both sides of the Dirac curve due to electron or hole conduction in the channel. These findings open the platform for further understanding the novel device concept of spin injection through 1D edge contact and for improvements of such device performance.

#### 3.1 Introduction

Spintronics provide an alternative approach for information processing and storage by utilization of another fundamental property of electrons other than electrical charge – its spin degree of freedom [11, 44–46]. Spin-based devices have the potential to be non-volatile, faster and have less energy consumption due to low switching energy between two logical states encoded in spin orientation of electrons. The heterogeneous integration of charge- and spin-based devices on one chip could potentially give rise to new boost of electronics development in the light of increasing scaling challenges due to shrinking logic and memory device dimensions.

Graphene has been shown to be a promising material for spintronics as an efficient

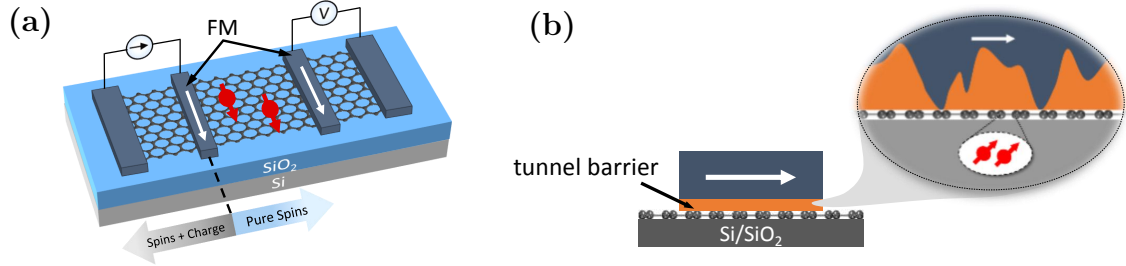


**Figure 3.1:** Conventional approach for spin injection/detection in graphene with surface top ferromagnetic contacts. (a) nonlocal spin valve device. White arrows indicate the direction of magnetization of ferromagnetic contacts, which can be changed to the opposite by the application of aligned external magnetic field. (b) Side view of injector/detector ferromagnetic contacts. Thin film of oxide tunnel barrier, which is essential for improved electrical spin injection from ferromagnet into graphene channel, contains pin-holes and surface roughness.

spin propagation medium due to low spin-orbit coupling and negligible hyperfine interactions [7,12–14]. Additionally, one can make heterostructures of graphene with other two-dimensional materials [4,5] which, in particular, open the possibilities of graphene sheet protection from environmental influences [33] and local enhancement of spin-orbit coupling in graphene due to proximity effects [12,47].

The main device configuration used to study spin transport is the nonlocal spin valve [14,48,49] in which charge bias circuit is separated from voltage detection circuit (Figure 3.1a). This has been utilized to distinguish between spin and charge transport signals and suppress spurious contributions from e.g. local Hall effects as well as to reduce the influence of device resistance fluctuations compared to the two-terminal spin valve device geometry.

The conventional approach utilizes metallization of graphene surface for fabrication of contacts which comprise of ferromagnetic (FM) material such as Co or permalloy deposited on top of thin tunneling barrier. The latter is important to mitigate the conductivity mismatch problem between spin transport medium and FM contact which lead to backscattering of spins into the latter and reduces spin accumulation under this contact [50–52].  $\text{AlO}_2$  [35,49],  $\text{TiO}_2$  [14] and  $\text{MgO}$  [53] are typical materials used as tunnel barriers for spin injection. However, deposition of atomically thin and smooth oxide tunnel barriers is very challenging. Hence, such thin films usually contain pin-holes, surface roughness, defects related to oxygen vacancies and in contact to graphene they cause doping of the latter [34,54] (Figure 3.1b). In the meantime, the 2D tunnel barrier of h-BN showing higher spin polarization has been developed [48]. However, with surface top contacts to graphene spins are injected and detected through  $\sim 1 \mu\text{m}$  wide contacts, averaging the effective spin injection efficiency. These factors can lead to additional spin dephasing and reduction of spin accumulation under the surface contacts [34,35].

Here, novel spintronic device design that utilizes 1D edge contacts [38] to graphene/hexagonal boron nitride (h-BN) heterostructures is proposed (Figure 3.2a). Such contacts design allows to ultimately reduce the interface area to graphene compared to surface contacts and consequently reduce the corresponding problems

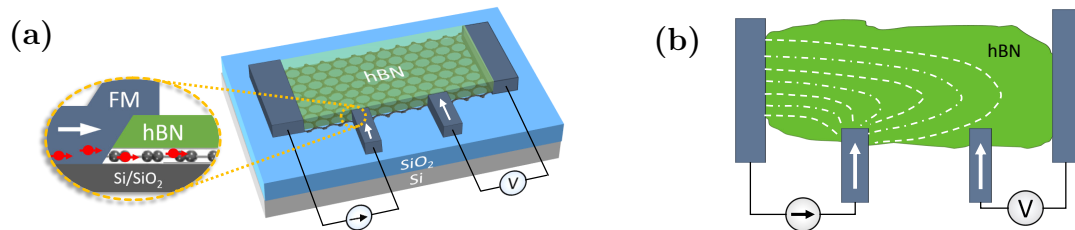


**Figure 3.2:** Novel nonlocal spin valve device concept with 1D edge ferromagnetic contacts to graphene. (a) Device design with enlarged region showing the spin injection from ferromagnetic contact into graphene channel for further transport and detection. (b) Qualitative picture of charge current spreading outside the bias circuit and reaching the nonlocal voltage detection circuit.

related to contacts-induced graphene doping and spin dephasing. Hence, such approach paves the path towards study of intrinsic graphene spin transport properties.

However, electrical injection of spins from ferromagnetic contact materials into single graphene layer through its 1D edge is a challenging task and requires understanding and optimization of the phenomena driving and influencing the operation of devices with such configurations of the contacts. This optimization is necessary both to enhance the spin signal and suppress any extraneous effects.

This chapter investigates the fabrication and operation of the nonlocal spin valve devices on graphene with 1D edge contacts. While aiming at the study of spin transport, magnetoresistance switching was observed which demonstrated behaviour not typical for spin signals. The observed behaviour is attributed to the local Hall effect. Its presence even in nonlocal geometry that was originally designed to suppress the influence of any spurious, not spin-related effects indicates that charge current spreading occurs outside the bias circuit (Figure 3.2b). This could be due to the specific spatial location of contacts from voltage detection circuit with respect to the path of charge flow. This study provides an insight into the phenomena that hinder spin-operation of nonlocal spin valve devices with 1D edge contacts and lay basis for further developments.

## 3.2 Results and discussion

The devices with 1D edge contacts to graphene/h-BN heterostructures were fabricated in the cleanroom using microfabrication process steps (Figure 3.3a). After the large-scale transfer of commercially available CVD graphene on Si/SiO<sub>2</sub> substrate (service of Graphenea [41]), the graphene was protected from the top by exfoliation of h-BN from bulk crystal using regular scotch-tape method. In the following etching step by oxygen plasma the flakes of exfoliated h-BN served as a mask for protection of graphene underneath from etching. Next, electron beam lithography process steps were utilized to define the resist mask for deposition of contact materials through electron beam evaporation of metals (1 nm TiO<sub>2</sub>/65 nm Co) followed by liftoff in acetone/IPA. The CVD graphene sheet in the fabricated device is electrically connected to the outputs via the 1D edge contacts [38]. Schematic representation and optical microscopy picture of the device are shown in Figure 3.3b and Figure 3.3c

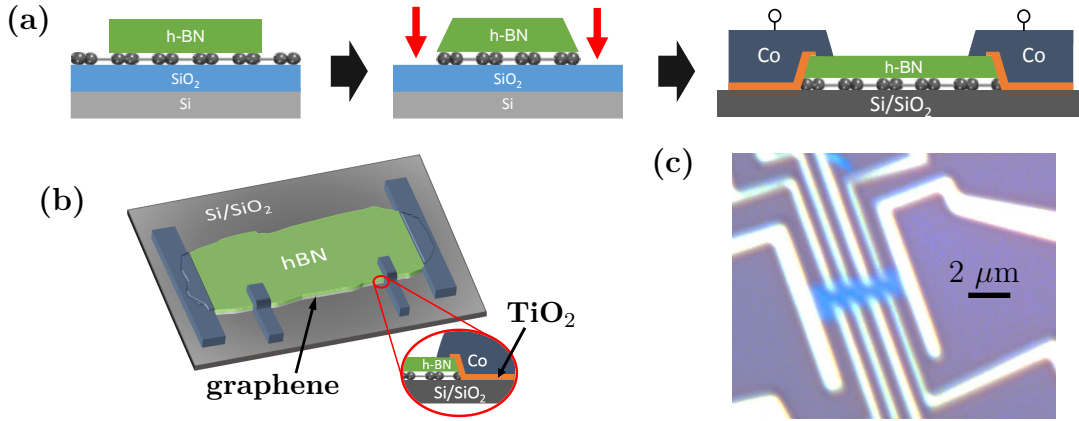


**Figure 3.3:** Fabrication of novel nonlocal spin valve device with 1D edge ferromagnetic ( $\text{TiO}_2/\text{Co}$ ) contacts to graphene/h-BN heterostructure. (a) Schematic of the fabrication process steps including preparation of heterostructures, their patterning and fabrication of contacts. (b) Schematic representation of the fabricated device and (c) optical microscopy picture.

respectively. The thickness of h-BN flakes on top of graphene is estimated to be  $\sim 25 \text{ nm}$ , which means that tunneling current from top part of the contacts can be neglected [55].

Characterization of graphene/h-BN heterostructure is depicted in Figure 3.4. The Raman spectrum of the graphene/h-BN heterostructure is shown in Figure 3.4a. The G and 2D peaks [56] related to graphene are visible at positions  $1568 \text{ cm}^{-1}$  and  $2632 \text{ cm}^{-1}$  respectively and h-BN peak [57] at  $1343 \text{ cm}^{-1}$ . Since the 2D peak is higher than the G peak and the former do not show band splitting one could conclude that the characterized graphene sheet is mostly monolayer [56]. The current-voltage (I-V) measurements revealed the edge contacts resistances to be in the range  $4\text{-}16 \text{ k}\Omega$ . The dependence of graphene sheet resistance on the back gate voltage applied to the silicon substrate was measured in local (Figure 3.4b) and nonlocal ( $R_{NL} = V_{NL}/I_{bias}$ ,

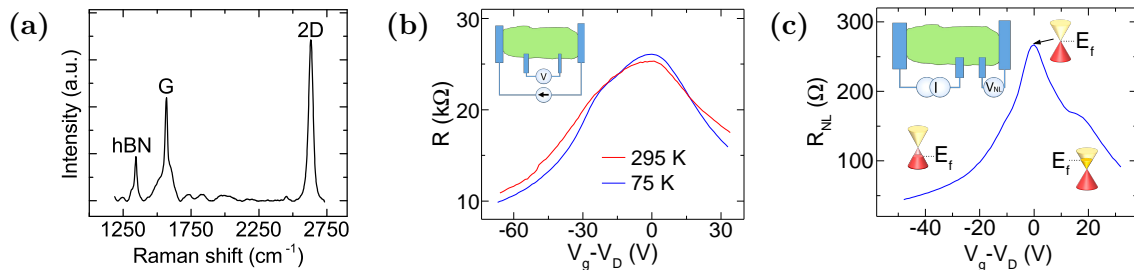


**Figure 3.4:** Characterization of graphene/h-BN heterostructures with 1D edge contacts. (a) Raman spectrum of graphene/h-BN heterostructure. (b) Graphene channel resistance as a function of back gate voltage ( $V_g$ )-Dirac point ( $V_D$ ) (Dirac curves) at  $295 \text{ K}$  (red) and  $75 \text{ K}$  (blue) for local measurement configuration (inset) and (c) at  $75 \text{ K}$  for nonlocal ( $R_{NL} = V_{NL}/I$ ) measurement configuration (inset) along with schematics of Dirac cones in graphene with positions of Fermi level at different regions of applied gate voltage.

Figure 3.4c) configurations. The graphene charge neutrality point was found to vary between different regions of graphene sheet and at different temperatures in the range from  $-5 V$  to  $+26 V$  of back gate voltage. The presence of measurable non-local voltage in the voltage detection circuit indicate that charge current spreading occurs outside the bias circuit (Figure 3.2b). The ohmic contribution ( $\sim R_s e^{-\pi L/w}$ ; where  $R_s$  – graphene sheet resistance,  $L$  and  $w$  – nonlocal channel length (separation between bias current and voltage detection contacts) and width of graphene channel respectively) [58] to this leakage was estimated to be  $\sim 25\Omega$  at charge neutrality point while the experimentally observed values were one order of magnitude larger. However, this comparison cannot exclude ohmic contribution to the observed non-local resistance as the main source of signal since analytical formula used is valid only for high aspect ratios  $L/w \gg 1$  of device geometry which is not the case for the measured sample ( $L/w \sim 1.7$ ).

The nonlocal spin valve device with such 1D edge contacts to graphene channel (Figure 3.2) was studied through sensitive magnetotransport measurements in liquid nitrogen cryostat under vacuum conditions of  $10^{-2} Torr$ . Sweeping the in-plane magnetic field aligned with the ferromagnetic contacts allowed to manipulate the direction of magnetization from parallel to anti-parallel due to uniaxial anisotropy. Fabrication of contacts of different widths allowed for tuning of the switching fields.

Nonlocal voltage  $V_{NL}$  was measured while sweeping the in-plane magnetic field aligned with the contacts at fixed bias currents (Figure 3.5). Single switching and hysteresis behaviour of  $V_{NL}$  was observed with symmetrical around the zero field voltage steps  $\Delta V_{\uparrow\downarrow}$  (top panel of Figure 3.5a). By changing the current direction, similar one-step switching signal with opposite sign of  $\Delta V_{\uparrow\downarrow}$  was observed.

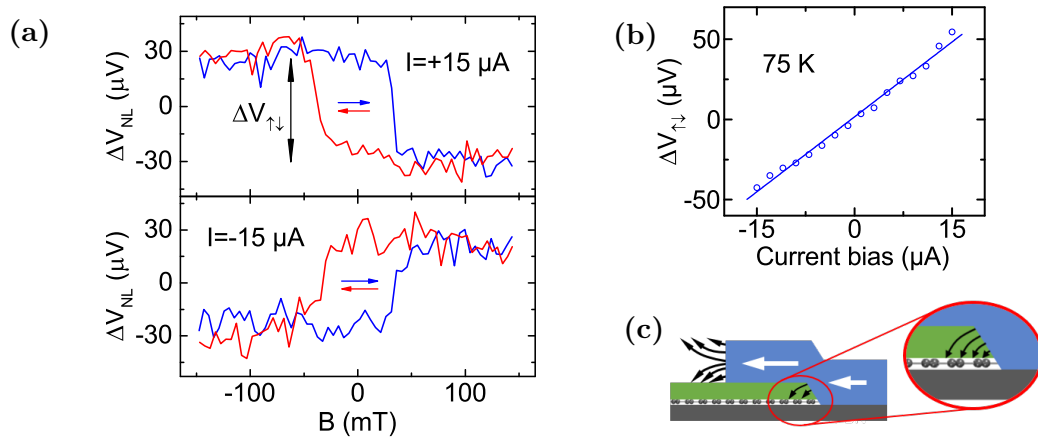


**Figure 3.5:** Magnetoresistance measurements of the spin valve device and bias dependence. (a) Measured nonlocal voltage as a function of applied external in-plane magnetic field aligned with the contacts at  $\pm 15 \mu A$  current bias at  $75 K$  for the left (red) and right (blue) sweep directions indicated by arrows. The baseline linear background voltage is subtracted. (b) Current bias dependence of the magnetoresistance signal switching of amplitude  $\Delta V_{\uparrow\downarrow}$  at  $75 K$ . (c) Schematics of the graphene/h-BN heterostructure near the 1D edge of ferromagnetic contacts showing the stray magnetic fields acting on graphene channel.

plete bias dependence of the signal is presented in Figure 3.5b, which show a linear dependence in the measured bias range. The presence of only one step of magnetoresistance for each sweep direction is not typical for spin signal [14, 49, 54, 59]. Taking into account that both contacts were fabricated together during the same fabrication process steps they are of similar quality and magnetic domain structure and, consequently, both should undergo the switching of their magnetization direction at corresponding applied coercitive magnetic field values. These values are typically within the sweeping field range for the corresponding dimensions of the fabricated contacts. If the observed magnetoresistance switching was due to spin transport in graphene channel, at least two steps would be visible for each sweep direction when both injector and detector contacts (the two middle contacts from bias and voltage detection circuits respectively in Figure 3.2a) switch the direction of their magnetization [14, 48, 49, 53].

Observed single switching in magnetoresistance response could be due to local Hall effect in the presence of stray magnetic fields emanating from the edges of ferromagnetic contacts (Figure 3.5c). It was previously observed in local measurement configurations with semiconductor [60–63] and graphene [35] channels. These stray fields create net perpendicular effective magnetic field near the edges of graphene and contact leads which can be as large as  $\sim 0.5 T$  [35, 60, 62] and they gives rise to the observation of the local Hall effect. The exact spatial distribution of stray fields depend on the magnetic domain structure near the edges of ferromagnetic contacts [60, 61]. As the amplitude of effective perpendicular component of stray magnetic fields quickly decays with distance  $d$  from the edge of ferromagnetic films ( $\langle B_{\perp} \rangle_{eff} \propto 1/(d^2 + h^2)$ ,  $h$  – film’s half thickness) [60], the contribution of stray fields in proximity to the graphene edge, where they are not separated by the h-BN, is more prominent (see enlarged region in Figure 3.5c). Such quick decay of stray magnetic fields with distance explains also their more prominent influence on the operation of spin valve devices with 1D edge contacts configuration compared to devices with surface contacts, where edges of ferromagnetic films are further away from the graphene channel.

Considering the local Hall effect as the dominant source of magnetoresistance switching and irregular geometry of investigated device (since otherwise the transverse Hall voltage would have no influence on the measured longitudinal nonlocal voltage), the measured  $V_{NL}$  can be written as linear combination of longitudinal ( $V_{xx}$ ) and Hall ( $V_{xy}$ ) voltages such that  $V_{NL} = aV_{xx} \pm bV_{xy}$ , where  $a$  and  $b$  are sample-specific coefficients [35]. The  $+$  and  $-$  signs here correspond to opposite directions of contacts’ magnetization (high and low magnetoresistance states respectively) while the  $V_{xx}$  could be due to ohmic leakage as discussed above. Since only one step in  $V_{NL}$  is observed one can assume that only one of the contacts in the voltage detection circuit cause measurable change in  $V_{NL}$  (when its magnetization is switched) within the resolution of measurement setup. Taking into account that the nonlocal resistance  $R_{NL}$  (see Figure 3.4c) due to current spreading should be much smaller at the reference contact (right contact in Figure 3.2b), the switching  $\Delta V_{\uparrow\downarrow}$  related to that contact is expected to be very low. Thus, the observed  $\Delta V_{\uparrow\downarrow}$  can be attributed to the left contact in the nonlocal voltage detection circuit. Considering the above mentioned contributions to  $V_{NL}$  the value of  $\Delta V_{\uparrow\downarrow}$  can be written

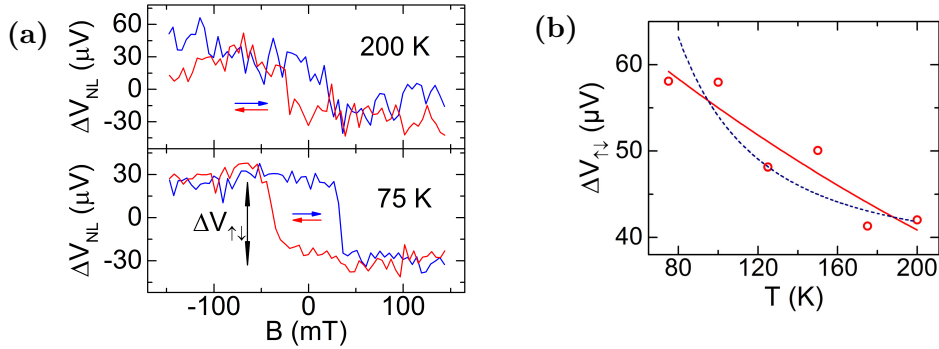


**Figure 3.6:** Temperature dependence of magnetoresistance signal. (a) Measured nonlocal voltage as a function of applied external in-plane magnetic field aligned with the contacts at 200 K (top panel) and 75 K (bottom panel) and at 15  $\mu A$  current bias for the left (red) and right (blue) sweep directions indicated by arrows. The background linear voltage is subtracted. (b) Temperature dependence of  $\Delta V_{\uparrow\downarrow}$  obtained from analysis of raw data at 15  $\mu A$  current bias (circles) along with the lead to the eye (solid line) and  $\propto 1/T^2$  fit (dashed line).

as  $\Delta V_{\uparrow\downarrow} = 2bV_{xy}$ . Taking into account that  $V_{xy} \sim I\langle B_{\perp}\rangle_{eff}/(en_{2D})$  [21, 23, 60, 64], the previous equation can be rewritten as

$$\Delta V_{\uparrow\downarrow} \approx 2b \frac{1}{en_{2D}} I \langle B_{\perp}\rangle_{eff} \quad (3.1)$$

where  $e$  – electron’s elementary charge,  $n_{2D}$  – sheet concentration of charges in graphene. This is in accordance with the measured linear dependence of  $\Delta V_{\uparrow\downarrow}$  on the amplitude and sign of current bias  $I$  (Figure 3.5b).

The temperature dependence of nonlocal spin valve signal  $V_{NL}$ , measured at a constant current bias of  $I = 15 \mu A$ , is presented in Figure 3.6. The observed voltage step  $\Delta V_{\uparrow\downarrow}$  decreased in amplitude with increasing temperature and was visible at up to 200 K at  $I = 15 \mu A$ . Such behaviour can be explained by considering Eq. (3.1) from which it implies that  $\Delta V_{\uparrow\downarrow} \propto 1/n_{2D}$ . Since the intrinsic charge carrier concentration in graphene is  $\propto T^2$  [65], one could expect the decrease of carrier concentration in graphene with decreasing temperature and, consequently, the increase of  $\Delta V_{\uparrow\downarrow}$ . Because some level of doping is always present in graphene, the experimental dependence of  $n_{2D}$  on  $T$  may deviate from the  $\propto T^2$ . Hence, the  $\Delta V_{\uparrow\downarrow}$  may deviate from  $\propto 1/T^2$  law and have less prominent temperature decay rate as it was observed (Figure 3.6b).

Graphene is a material where concentration of charge carriers and even their type can be tuned by the application of gate voltage. This was utilized to study the gate voltage dependence of observed magnetoresistance switching (Figure 3.7). The measurements revealed clear correlation between the sign of  $\Delta V_{\uparrow\downarrow}$  and type of charge carriers (electrons and holes) in graphene (Figure 3.7a). The absolute value of  $\Delta V_{\uparrow\downarrow}$  demonstrated peaks near the charge neutrality point in graphene and its sign was found to be opposite for electron- and hole-type of charge carriers. This is also clearly visible in Figure 3.7b where the application of back gate voltage  $V_g = \pm 30 V$  (which corresponds to electron- or hole-type of graphene channel con-

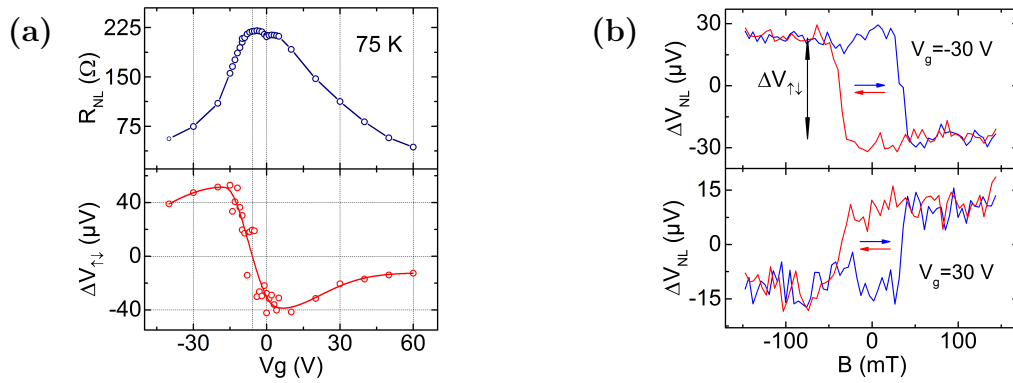


**Figure 3.7:** Gate dependence of magnetoresistance signal. (a) Back gate dependence of nonlocal graphene resistance  $R_{NL} = \langle V_{NL} \rangle / I$ , where  $\langle V_{NL} \rangle$  – baseline nonlocal voltage extracted from sweeps of in-plane magnetic field aligned with the contacts (top panel) and analyzed nonlocal voltage steps  $\Delta V_{\uparrow\downarrow}$  (bottom panel). (b)  $V_{NL}$  as a function of in-plane external magnetic field sweeps at  $-30$  V (top panel) and  $+30$  V (bottom panel) of applied gate voltage with subtracted baseline voltage offset. In (a) and (b) current bias is  $15 \mu A$  and measurements were performed at  $75$  K.

duction) changed the sign of magnetoresistance (sign of  $\Delta V_{\uparrow\downarrow}$ ). The peaks of  $\Delta V_{\uparrow\downarrow}$  near the charge neutrality point, where the graphene concentration is minimal, as well as the change of sign of  $\Delta V_{\uparrow\downarrow}$  for electron- and hole-type of graphene conduction (with opposite signs of  $n_{2D}$ ) correlates with Eq. (3.1). These experiments support the argument in favor of local Hall effect-dominated magnetoresistance switching. At the same time this gives additional argument to rule out the spin-related nature of the observed switching since magnetoresistance signal because of spin transport do not change sign with the change of charge carriers type and its amplitude weakly depends on the applied gate voltage [49]. One should also notice the clear similarity between the measured  $\Delta V_{\uparrow\downarrow}$  dependence on gate voltage ( $\Delta V_{\uparrow\downarrow} \propto V_{xy}$  or local Hall voltage according to Eq. (3.1)) and the corresponding dependence of regular Hall voltage measured in Hall bar geometry (see bottom panel of Figure 4.5b in the next chapter). This similarity can be justified by the same nature of local and regular Hall effects due to Lorentz force acting on moving charges in the presence of perpendicular external or stray magnetic fields.

The performed analysis of raw data point to the local Hall effect-dominated phenomena which results in magnetoresistance switching observed in nonlocal measurement geometry with 1D edge contacts to CVD graphene. In order to suppress such extraneous effects and enhance the spin injection into the graphene channel several improvements are suggested.

First, for reduction of the current spreading and ohmic contributions ( $\sim e^{-\pi L/w}$ ), the increase of separation between bias circuit and nonlocal voltage detection circuits  $L$  as well as improvement of graphene properties, such as mobility and sheet resistance, would be beneficial. The improved graphene properties would also be useful for long distance spin transport in graphene. Additionally, the geometry of graphene sheet can be reconsidered to be of shirking width with distance from the left reference contact to suppress spins from diffusing in undesired directions and,

again, reduce current spreading.

Next, to decrease the effective perpendicular magnetic field component of stray fields  $\langle B_{\perp} \rangle_{eff}$ , graphene should be completely encapsulated by h-BN from the top and bottom. This would not only provide an atomically flat, better-quality substrate for graphene [33] compared to SiO<sub>2</sub>, but also reduce  $\langle B_{\perp} \rangle_{eff}$  near graphene edges since in that case fringe fields from ferromagnetic contacts would be acting on graphene sheet from the bottom and the top in opposite directions, thus partly compensating each other.

Finally, to enhance the injection of spins into graphene using edge contacts by electrical means, multilayer graphene channel with increased area of edge contacts could be considered. This would also provide an additional benefit of decreased spin dephasing in the transport channel due to screening of scattering potentials [66].

### 3.3 Conclusions

In summary, the operation of the novel nonlocal spin valve device with 1D edge contacts was investigated. The device was fabricated on large area CVD graphene on Si/SiO<sub>2</sub> substrate, protected by exfoliated h-BN on top. The prepared graphene/h-BN heterostructures were characterized by Raman spectroscopy and gate dependence of graphene resistance. While aiming at the study of spin transport in graphene in the novel device configuration with 1D edge contacts to graphene, sweeping the in-plane external magnetic fields aligned with the contacts revealed magnetoresistance switching not typical for spin signals. The observed behaviour is attributed to local Hall effects in the presence of stray magnetic fields from ferromagnetic contacts. The measured back gate voltage dependence of magnetoresistance allowed to rule out spin-related nature of observed signal, while current bias and temperature dependencies were also found to be in accordance with the local Hall effect. This study provide insight into the operation of spin valves with novel device design and lay basis for further developments.



## Chapter 4

# Gate-tunable magnetic Hall sensors on large area CVD graphene protected by exfoliated h-BN and with 1D edge contacts

Graphene is an excellent material for Hall sensors because of its atomically thin structure, high carrier mobility and low carrier density. However, graphene devices need to be protected from environment for reliable and durable performance. This chapter focuses on investigation of Hall sensors fabricated on large area commercially available CVD graphene with protection by exfoliated hexagonal boron nitride (h-BN). The prepared graphene/h-BN heterostructures show good materials properties as characterized by Raman spectroscopy. To connect the graphene active regions of Hall samples to the outputs the 1D edge contacts were used which show reliable and stable electrical properties. The operation of Hall sensors shows the current-related sensitivity up to  $366 \text{ V}/\text{AT}^{-1}$  and the measurements of magnetic field down to millitesla range. The ability to change carrier concentration and type of charge carriers (n- or p-type) in graphene by the gate voltage is demonstrated by the gate tunability of the Hall sensitivity.

### 4.1 Introduction

Magnetic field sensors today represent a significant growing market estimated to reach annual shipment of up to 9.6 billion units by 2020 [24] and 3.65 billion in value terms by year 2022 [25]. The areas of application cover many fields such as automotive, consumer electronics, healthcare, defense industry and others, where magnetic field sensors are used for position detection, current monitoring, angular sensing, among others [21–23]. Many different magnetic sensors based on a variety of effects have been realized for different applications (Figure 4.1 [67]). With a share of over 55% in 2014 [25], Hall effect based sensors, utilizing semiconductors in the active region and used for magnetic field detection in the field range from  $10^{-7} \text{ T}$  to  $10^2 \text{ T}$  (Figure 4.1) and temperature range from  $-40 \text{ }^\circ\text{C}$  up to  $150 \text{ }^\circ\text{C}$  [18, 23, 68], constitute a significant part of the industry. Due to the low fabrication cost, highly developed processing technology, good integration into signal processing circuits and reasonable performance properties (current normalized sensitivity  $S_I \sim 100 \text{ V}/\text{AT}^{-1}$ ) [22, 23, 29, 30], the active region today in such sensors is mostly represented by Si. Hall sensors based on III-V compound semiconductors and 2D electron gas with semiconductor heterostructures [15, 21, 26–28] provide better sensitivities, but they are expensive

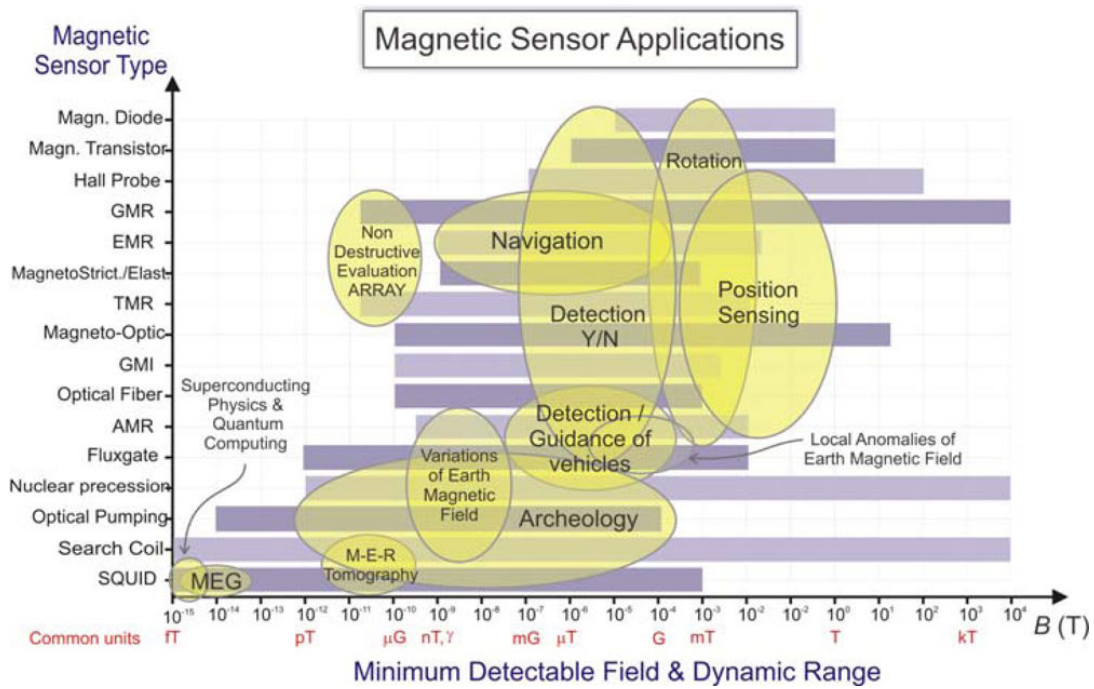


**Figure 4.1:** An overview of the field of magnetic sensors and their applications with corresponding detectable magnetic field ranges [67].

and more difficult to integrate in the circuits.

Owing to its 2D nature, low carrier concentration  $n_{2D}$  and high mobility  $\mu$ , graphene is highly interesting material to be used in the active region of magnetic Hall sensors with performances reaching or even outpacing those of III-V compounds-based Hall sensors. Recent reports on graphene-based Hall sensors with exfoliated flakes suggested very good operations reaching up to  $5700 \text{ V/AT}^{-1}$  and  $3 \text{ V/VT}^{-1}$  current-related ( $S_I \propto 1/n_{2D}$ ) and voltage-related ( $S_V \propto \mu$ ) sensitivities respectively [17]. Additionally, high linearity [15, 16] and low noise [16, 18, 69] also provide the high potential of graphene for the use in magnetic Hall sensors. Moreover, one can make flexible graphene sensors [19, 20] by putting them on flexible substrates such as kapton foil.

However, the ultra-sensitive graphene sensor devices demonstrated either exploit exfoliated graphene flakes or are made of a manually selected single crystal CVD graphene area, or the graphene active layer is not protected from external influences for robust device operation [17, 19, 33]. Thus, there is a necessity to investigate graphene magnetic Hall sensors fabricated on large area CVD graphene and with protection of the single graphene layer. Unprotected, graphene is very prone to defects introduced during fabrication processes and also defects introduced due to interfaces with other insulators or contact materials. These defects can deteriorate graphene properties, cause uncontrolled doping leading to increased carrier concentration and, consequently, reduced sensitivities [15, 22, 68] and increased noise [16, 69].

In this chapter, magnetic Hall elements fabricated on large area CVD graphene covered on top with hexagonal boron nitride (h-BN) are investigated. The h-BN is another insulating atomically flat 2D material with good interface properties to

graphene containing low amount of dangling bonds and charge traps [33]. It is used for protection of graphene and reduces degradation of graphene channel properties. By ultimately reducing the contact area, the device scheme used with 1D edge contacts to graphene also allows to circumvent the effects related to contact-induced doping of graphene, which is important for high current-related sensitivity of Hall sensors.

## 4.2 Results and discussion

The Hall sensor devices were fabricated on commercially grown CVD graphene transferred on Si/SiO<sub>2</sub> substrate by Graphenea company [41]. The micro-fabrication process steps are depicted in Figure 4.2a. The h-BN flake was exfoliated from bulk crystal on top of graphene by means of a regular scotch-tape method. Then the unprotected graphene regions were etched away with oxygen plasma. 1D edge contacts [38], which are used to electrically connect Hall elements to the outputs, were fabricated by means of electron beam lithography and electron beam evaporation of metal contacts (1 nm TiO<sub>2</sub>/65 nm Co) followed by liftoff in acetone/IPA. Schematically the investigated sample is represented in Figure 4.2b and the optical microscopy picture of the device is shown in Figure 4.2c. The length and width of the active region of the device 4.1 μm and 1.2 μm respectively.

Figure 4.3 shows the characterization of graphene/h-BN heterostructure and 1D edge contacts to graphene. The Raman spectrum of the graphene/h-BN heterostructure is shown in Figure 4.3a with graphene G and 2D peak [56] positions at 1570 cm<sup>-1</sup> and 2636 cm<sup>-1</sup> respectively and h-BN peak [57] at 1344 cm<sup>-1</sup>. The absence of band splitting of 2D peak of graphene and its relative higher intensity than the G peak indicate that graphene in the heterostructures is monolayer [56]. The typical two-terminal current-voltage (I-V) characteristic at room temperature

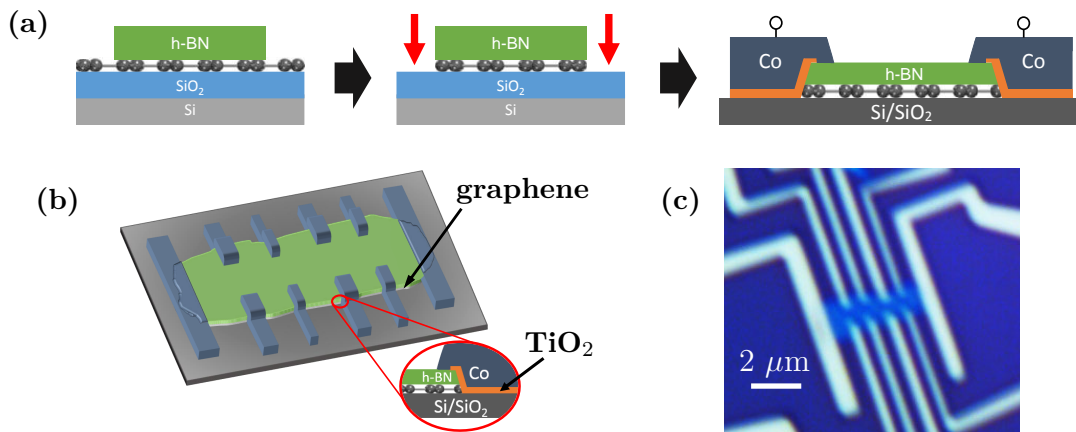


**Figure 4.2:** Fabrication of CVD graphene/h-BN heterostructures with 1D edge contacts. (a) Schematics of the fabrication process steps involving the preparation of graphene/h-BN heterostructures, followed by patterning and formation of 1D edge contacts.(b) Schematic representation and (c) optical microscopy picture of the fabricated device.

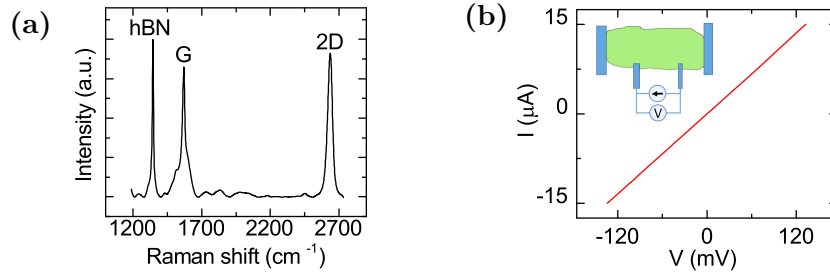


**Figure 4.3:** Characterization of CVD graphene/h-BN heterostructures and 1D edge contacts. (a) Raman spectrum of graphene/h-BN heterostructure. (b) Typical 2-terminal IV characteristic of the 1D edge contacts to graphene at room temperature. Inset: measurement configuration.

(figure 4.3b) shows a linear behaviour and contact resistances fall in the range from  $4\text{ k}\Omega$  to  $16\text{ k}\Omega$ .

Hall sensors exploit the Hall effect according to which perpendicular magnetic field to the conducting plane deflect the moving charges in transverse direction and cause the build up of potential difference called the Hall voltage  $V_H$ . This is described by the linear equation [21, 23, 64]:

$$V_H = \frac{1}{en_{2D}}IB + V_{offset} \quad (4.1)$$

where  $B$  – perpendicular magnetic field,  $e$  – elementary electron charge,  $n_{2D}$  – sheet concentration of charges in graphene,  $I$  – bias current and  $V_{offset}$  – background voltage offset, present due to the horizontal misalignment between the two Hall probe contacts. Thus, from the measured Hall voltages current-related sensitivities ( $S_I$ ) of Hall sensors, which are among the most important operation parameters of these devices, can be extracted using the following equation [15, 21, 23]:

$$S_I = \left. \frac{1}{I} \frac{\partial V_H}{\partial B} \right|_{I=const} \quad (4.2)$$

The Hall measurements were performed on the studied device (Figure 4.4a) using the measurement configuration depicted in the inset. From the linear fitting using Eq. (4.1) graphene was found to have the p-type conduction at zero back gate voltage with sheet concentration of charges of  $1.75 \times 10^{12}\text{ cm}^{-2}$  and background Hall voltage offset of  $3\text{ mV}$  at  $15\text{ }\mu\text{A}$  current bias, which has been subtracted from the measured raw data. The linearity error [15, 23, 28] is around the average level of  $1.6\%$  at room temperature. Based on the Figure 4.4b, where the Hall voltage response is measured as a function of time at different perpendicular magnetic fields, one can find that the minimum magnetic field of  $\sim 20\text{ mT}$  can be resolved from the noise at room temperature and  $15\text{ }\mu\text{A}$  current bias. Recent studies suggested that the noise in graphene magnetic Hall sensors at low frequencies is largely due to flicker noise [16–18, 69]. The spectral power density of such noise is inversely proportional to the area of the active region and strongly reduces with increased mobility of graphene channel. Hence, one can improve minimum magnetic field resolution

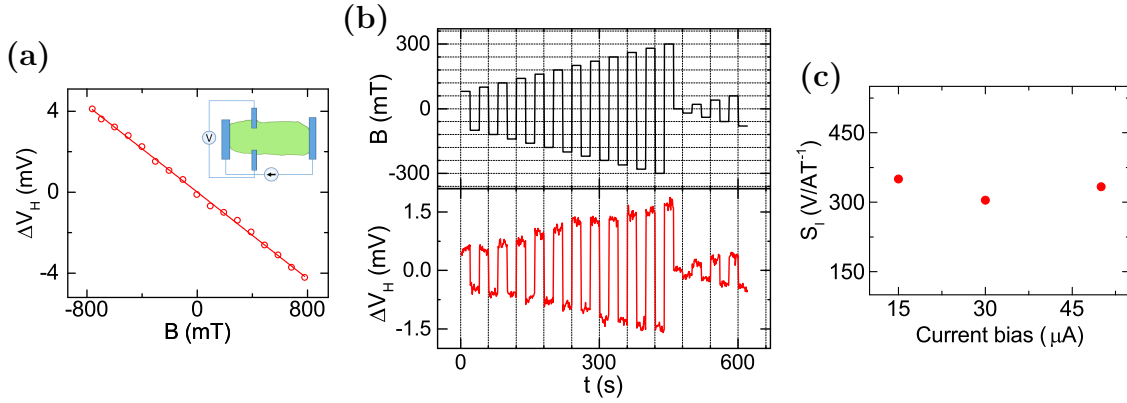


**Figure 4.4:** Operation of CVD graphene/h-BN Hall elements. (a) Output Hall voltage as a function of perpendicular magnetic field at 294 K (circles) along with linear fitting (solid line) according to equation 4.1. Inset: measurement configuration. (b) Output Hall voltage as a function of time at different applied magnetic fields at room temperature. (c) Current-related sensitivity as a function of current bias. In (a) and bottom panel of (b) applied current bias is  $15 \mu\text{A}$  and Hall voltage is subtracted by the background offset value.

by increasing mobility and area of active region. Additionally, the resolution can be further increased by lowering the thermal (Johnson–Nyquist) noise contribution at lower temperatures. The current-related Hall sensitivity, calculated using equation 4.2, showed a stable bias dependence in the range from  $15 \mu\text{A}$  to  $50 \mu\text{A}$  at room temperature (Figure 4.4c).

Next, the Hall sensitivity of graphene in electron and hole doped regions and also for different carrier concentrations was investigated. Graphene is a unique Dirac material, where charge carrier type and concentration can be tuned by application of gate voltage. This was utilized to investigate the gate tunability of operation of Hall sensors at room temperature and 70 K (Figure 4.5 and Figure A.1 respectively). Figure 4.5a demonstrates the change of type of conduction from electrons to holes in the graphene channel by application of gate voltage  $V_g = \pm 40 \text{ V}$  and thus change of the sign of slope of Hall response. From the back gate dependence of graphene resistance the charge neutrality point was found at  $V_g = 26 \text{ V}$ . Such full gate-dependent Hall effect measurements were performed by sweeping back gate voltages from electron to hole type of conduction across the Dirac point in the presence of different perpendicular magnetic fields under  $15 \mu\text{A}$  of current bias (bottom panel of Figure 4.5b). To reduce the influence of the device geometry and measurement setup, in Figure 4.5b (bottom panel) the measured response at magnetic field of  $0 \text{ T}$  ( $V_{H0}$ ) was taken as a reference and subtracted from the Hall response at other magnetic fields ( $V_H(B)$ ) according to the formula  $\Delta V_H = V_H(B) - V_{H0}$  [17]. Here, one can see that the amplitude  $\Delta V_H$  is changing with the applied gate voltage pointing to the change of sensitivity of Hall element. Indeed, the extracted current-related sensitivity from fitting of  $\Delta V_H$ - $B$  dependencies using Eq. (4.2) (with  $\Delta V_H$  instead of  $V_H$ ), plotted in Figure 4.5c as a function of gate voltage, reveal the gate voltage-induced changing of absolute value of sensitivity with peaks close to the charge neutrality point of graphene and reaching up to  $\sim 345 \text{ V/AT}^{-1}$  at room tem-

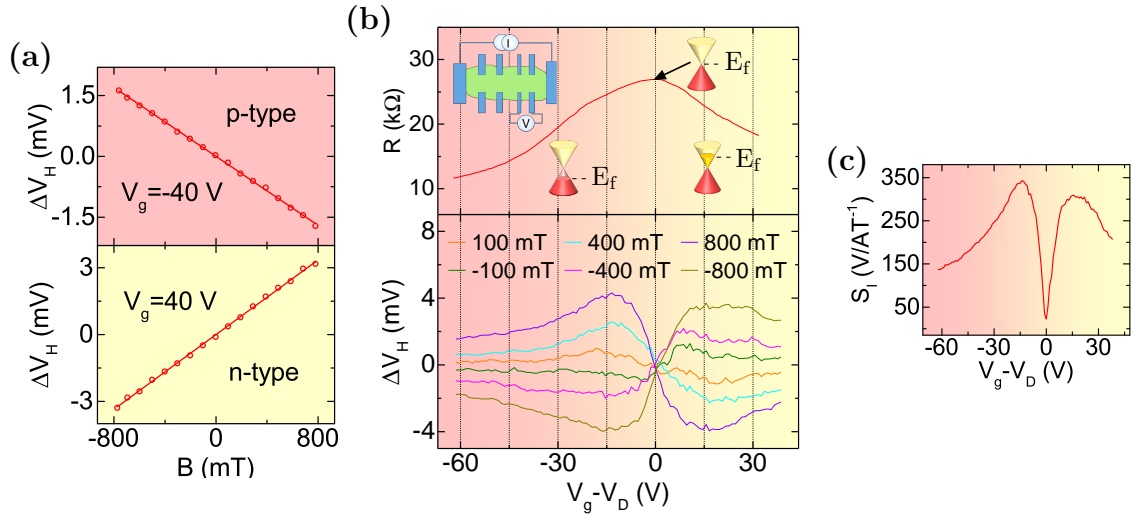


**Figure 4.5:** Gate tunability of CVD graphene/h-BN Hall sensors' operation. (a) Output Hall voltage as a function of perpendicular magnetic field strength at  $-40$  V (top panel) and  $+40$  V (bottom panel) applied to the back gate with subtracted background voltage offset. (b) Back gate dependence of graphene resistance (top) and Hall voltage response as a function of back gate voltage at different perpendicular magnetic fields with subtracted response at  $0$  T of applied field (bottom). Measurement configuration for top panel is shown in the inset along with schematics of Dirac cones in graphene with positions of Fermi level at different regions of applied gate voltage. (c) Absolute value of current-related sensitivity calculated from bottom panel of (b) according to equation 4.2 as a function of gate voltage. In all plots current bias is  $15 \mu\text{A}$  and measurement are shown at room temperature. Gradients of background color indicate the transition of graphene conduction from p-type (pink) to n-type (yellow). The horizontal axes are centered around the charge neutrality point in (b) and (c). Measurement configurations in (a) and bottom panel of (b) are the same as depicted in the inset of Figure 4.4a.

perature and  $\sim 366 \text{ V}/\text{AT}^{-1}$  at  $75 \text{ K}$  (Figure A.1b). Such tunability of Hall response stems from gate voltage-induced change of the carrier concentration in the graphene sheet yielding a change of current-related sensitivity and output Hall voltage (see Eq. 4.1 and Eq. 4.2).

The observed Hall sensitivities could be further increased by improving the graphene properties and by reducing the  $\text{SiO}_2$  substrate-induced doping and interactions by formation of h-BN/graphene/h-BN heterostructures [15, 70]. In order to advance the technology of fabrication of magnetic Hall sensors towards practical applications, sensors fabricated only on large area CVD graphene and CVD h-BN heterostructures should be considered. However, the present sensitivities of the CVD graphene/h-BN heterostructure-based Hall sensors are at least three times higher than silicon-based devices and have the additional advantage to be used in transparent and flexible electronics.

### 4.3 Conclusions

In summary, the operation of graphene magnetic Hall sensors fabricated on large area graphene on Si/SiO<sub>2</sub> substrate, protected with h-BN on top and with 1D edge contacts, is demonstrated in this chapter. Such encapsulated devices showed reliable contact properties and Hall sensor performance over a longer time period and are promising for operation in ambient conditions. The samples show a stable bias dependence of current-related sensitivity and a magnetic field resolution at room temperature of  $\sim 20$  mT. A current-related sensitivity up to  $366$  V/AT<sup>-1</sup> with little temperature-related change was observed. A gate voltage-induced tunability of the Hall response has been demonstrated with changing absolute value and sign of current-related sensitivity. A further increase of the sensitivity and application potential of graphene-based magnetic Hall sensors is possible by using high-quality graphene fully encapsulated with h-BN, prepared by all-CVD growth methods over large area. This is the main focus of the next chapter, where batch fabrication of all-CVD h-BN/graphene/h-BN heterostructures-based magnetic Hall sensors with 1D edge contacts is developed.



## Chapter 5

# Magnetic Hall sensors batch-fabricated on all-CVD graphene/h-BN heterostructures with 1D edge contacts

Graphene, due to its high mobility and low carrier concentration, is highly promising atomically thin material that could potentially replace widely used today's Si-based Hall sensors. In this chapter, the scalable fabrication of Hall sensors on large area graphene encapsulated in hexagonal boron nitride (h-BN) using only commercially available CVD materials is demonstrated. The h-BN/graphene/h-BN stacks were prepared by layer transfer technique batch-fabricated by utilizing 1D edge contacts to graphene. The devices showed robust performance over the chip scale with tunneling characteristics of the edge contacts. Magnetic Hall sensitivity down to millitesla range is observed at room temperature with current-related sensitivities up to  $97 \text{ V/AT}^{-1}$ . This work opens avenues for more mature technology of fabrication of all-CVD h-BN/graphene/h-BN heterostructures-based Hall elements for industrial implementation.

### 5.1 Introduction

As explained in section 4.1, the market size of magnetic sensors today is significant with projected growth in the coming years and an important part of this industry is occupied by the Hall effect-based magnetic sensors. Recent reports [15–17, 20] prove the high potential of graphene in the field of magnetic Hall sensors, but they all lack either scalability of fabrication process or protection of graphene channel for industrial scale production.

Chapter 4 describes the operation of graphene Hall elements fabricated on large area graphene with top exfoliated h-BN protection. The work described in this chapter takes one step further towards advancing this technology and towards the ambition of bringing it into the market by exploiting scalable fabrication approach with the use of only commercially available CVD materials with active region consisting of graphene protected from the top and bottom by h-BN to preserve the unique beneficial graphene properties from deterioration. The 1D edge contacts to graphene [38] are utilized for contacting graphene active region. They allow to circumvent the restrictive requirement for sequential layer assembly of graphene/h-BN heterostructures (since no process of selective etching of only h-BN is available)

during the fabrication process for exposing the surface of graphene for metallization in contrast to top contacts [38]. Such large-scale batch fabrication of h-BN-encapsulated graphene Hall elements can bring the technology closer to industrial production.

## 5.2 Results and discussion

The samples were prepared by using industry-compatible large-scale fabrication techniques. The schematic representation of investigated devices is shown in Figure 5.1a. Figure 5.1b presents the optical microscopy picture of the typical graphene Hall element of the larger size.

The devices were batch-fabricated through the micro-fabrication process as shown schematically in Figure 5.1c. Each Hall element consist of graphene sandwiched between 13 nm thick multilayer h-BN. Both materials are commercially produced (graphene from Graphenea [41] and h-BN from Graphene Supermarket [42]) CVD-grown on copper substrate and were wet-transferred on Si/SiO<sub>2</sub> substrate using standard PMMA-assisted process [59] to form heterostructures (the large wafer scale transfer process – service of Graphenea). The aluminum (20 nm) hard mask was patterned by means of laser writer followed by etching of the uncovered heterostructure regions with CHF<sub>3</sub> in the presence of oxygen flow. Then the Al hard mask was removed by wet chemical etching step. After the heterostructures patterning contacts were fabricated by means of electron beam lithography and electron beam evaporation of metals (20 nm Ti/60 nm Au) following by liftoff in acetone. Thus, the encapsulated graphene active region is electrically contacted through 1D edge contacts [38] (Figure 5.1c).

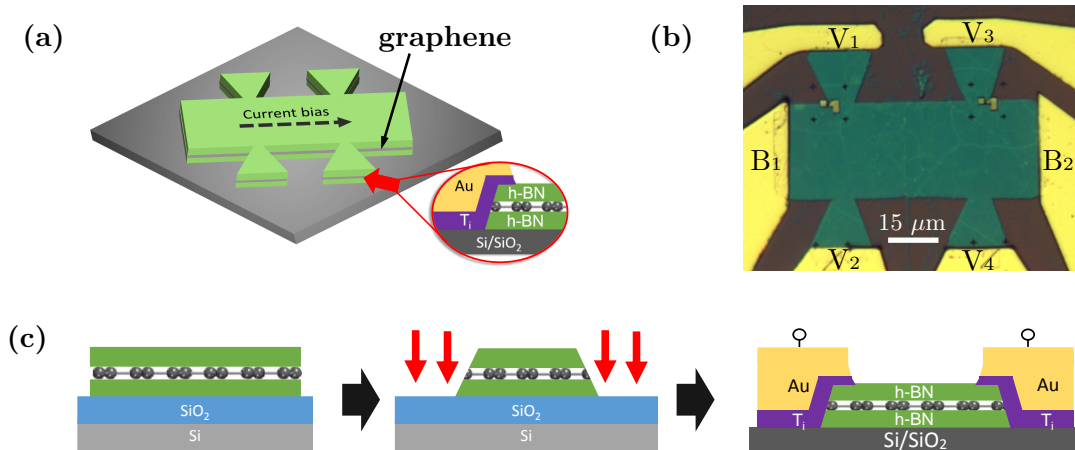


**Figure 5.1:** Fabrication of magnetic Hall elements based on large area CVD graphene encapsulated in CVD h-BN on Si/SiO<sub>2</sub> substrate. (a) The schematic representation of the fabricated Hall sensor devices with h-BN/graphene/h-BN heterostructure and 1D edge contacts. (b) Optical microscopy picture of a typical graphene Hall element with a scale bar of 15 μm. (c) Schematic of the fabrication process steps involving the preparation of h-BN/graphene/h-BN heterostructures by layer transfer method, followed by patterning and formation of 1D edge contacts.

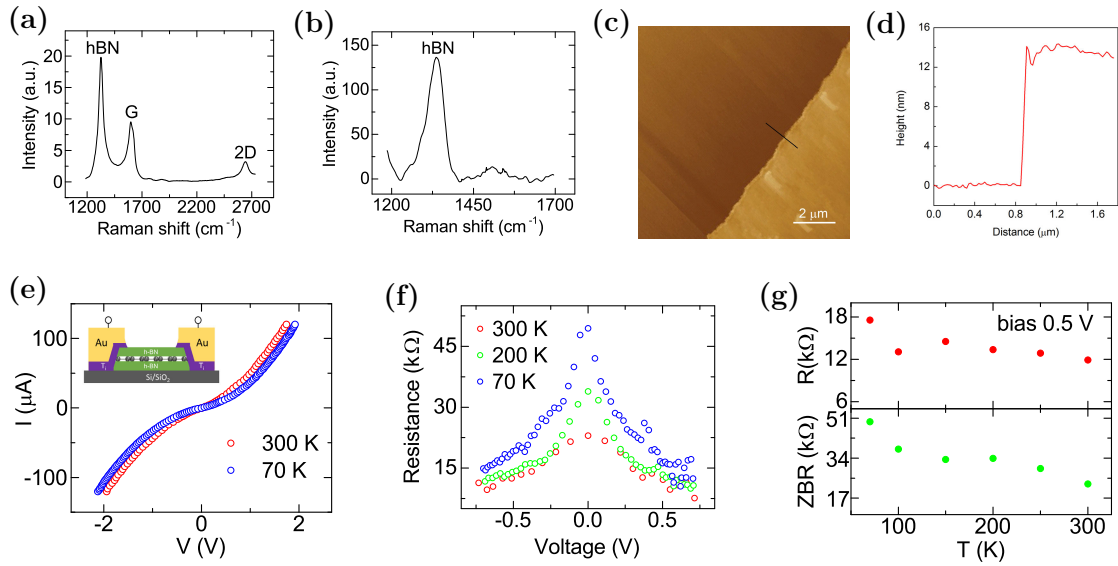


**Figure 5.2:** Characterization of the heterostructures and 1D contacts. (a) Raman spectrum of h-BN/graphene/h-BN heterostructures. (b) Raman spectrum of only CVD h-BN after transfer on Si/SiO<sub>2</sub> substrate. (c) Typical AFM image and (d) AFM thickness profile of the utilized CVD h-BN (courtesy of Graphene Supermarket [42]). (e) 2-terminal IV characteristic measured at 300 K (red) and 70 K (blue). Inset: schematics of the measurement configuration. (f) 2-terminal resistance as a function of voltage drop at different temperatures of 70 K (blue), 200 K (green) and 300 K (red). (g) Corresponding resistance at 0.5 V bias (top) and zero bias voltage (bottom) as a function of temperature.

The properties of the all-CVD h-BN/Graphene/h-BN heterostructures in the active region of Hall sensors connected through 1D edge contacts were investigated by Raman and electrical transport measurements. Figure 5.2a depicts typical Raman spectrum for the heterostructures with G and 2D graphene peaks [56] at  $1598\text{ cm}^{-1}$  and  $2643\text{ cm}^{-1}$  correspondingly and h-BN peak [57] at  $1326\text{ cm}^{-1}$  for 638 nm laser excitation wavelength. The stronger intensity of G peak than the 2D peak is not typical but was observed previously in high-contrast regions of CVD-grown on copper and transferred on Si/SiO<sub>2</sub> substrate misoriented or turbostratic

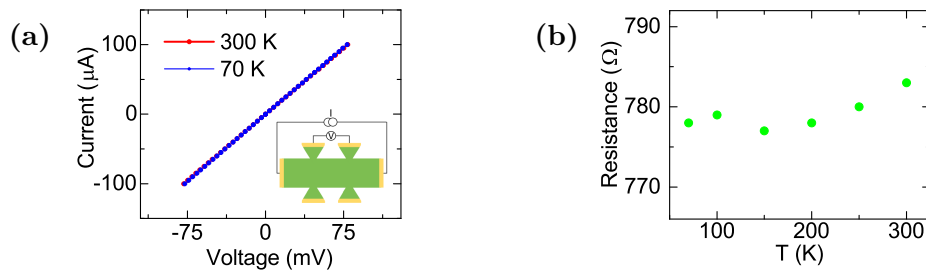


**Figure 5.3:** Graphene channel characterization. (a) Typical IV characteristic of encapsulated graphene active region at 300 K (red) and 70 K (blue). Inset: the measurement configuration. (b) Temperature dependence of graphene resistance.

multilayer graphene [71], which indicates that the region of graphene where Raman spectrum was measured could be multilayer. The Raman spectrum for only CVD h-BN is depicted in Figure 5.2b. As one can see from AFM image in Figure 5.2c and AFM height scan in Figure 5.2d (courtesy of Graphene Supermarket [42]), the CVD h-BN is multilayer and the typical thickness is  $\sim 13\text{nm}$ . This means that the tunneling current through h-BN from the part of the contact lead which overlaps the heterostructures on top can be neglected. Figure 5.2e shows typical tunneling current-voltage (I-V) characteristic for 2-terminal measurement configuration (presented in the inset of Figure 5.2e) with 1D edge contacts between graphene and Ti/Au with resistances around  $10\text{ k}\Omega \times \mu\text{m}$ . The corresponding differential resistance in Figure 5.2f shows peaks at zero voltage, which increase with decreasing temperature. This, together with weak temperature dependence [72] of resistance at zero bias and at  $0.5\text{ V}$  bias shown on Figure 5.2g, indicate the tunneling behavior at the interface of the edge contact. One should notice that graphene could not be the cause of such behavior of 2-terminal IV characteristic and temperature dependence of resistance as it implies from Figure 5.3 where no tunneling is observed with linear IV characteristic (Figure 5.3a) and negligibly weak temperature dependence of graphene channel resistance (Figure 5.3b). The barrier at the 1D edge contact could be present due to interfacial species incorporated during etching of the h-BN/graphene/h-BN stack and graphene termination chemistry [38] as well as oxidation of Ti in the contacts in proximity to h-BN/graphene/h-BN stack due to residual oxygen at the interface. The sheet resistance  $R_s$  of encapsulated CVD graphene, calculated according to the formula  $R_s = R/N_{sq}$  [64] with  $N_{sq}$  – the number of squares that one can fit into the measured graphene channel region with resistance  $R$ , was estimated to change from  $520\ \Omega/\square$  to  $870\ \Omega/\square$  (see Figure 5.4a).

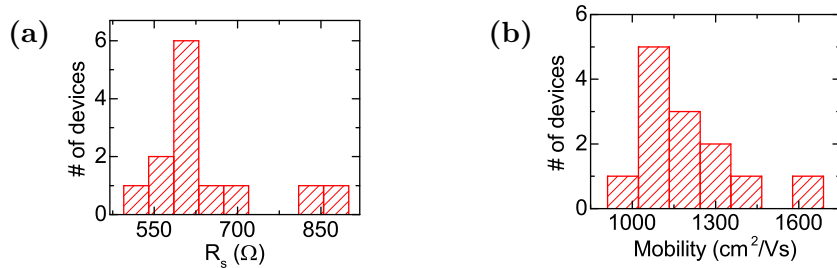


**Figure 5.4:** The distribution of (a) sheet resistance and (b) Hall mobility of h-BN-encapsulated graphene within a batch of 13 graphene Hall elements. The most common values of mobility and sheet resistance are  $\sim 1080\text{ cm}^2/\text{Vs}^{-1}$  and  $\sim 610\ \Omega/\square$ , correspondingly

Using the measurement configuration depicted in the inset of Figure 5.5a, the voltage difference (Hall voltage) accumulated in the transverse direction in the presence of perpendicular magnetic field due to the Lorentz force acting on the moving charges in graphene was measured. The output linear Hall voltage as a function of applied magnetic field measured at bias current of  $90\ \mu\text{A}$  is shown in Figure 5.5a. A very weak temperature change is observed within the range of  $70 - 300\text{ K}$ . The background voltage offset was found to be in the range from  $4\text{ mV}$  to  $7\text{ mV}$  at  $90\ \mu\text{A}$  bias and was present due to horizontal misalignment between Hall probe

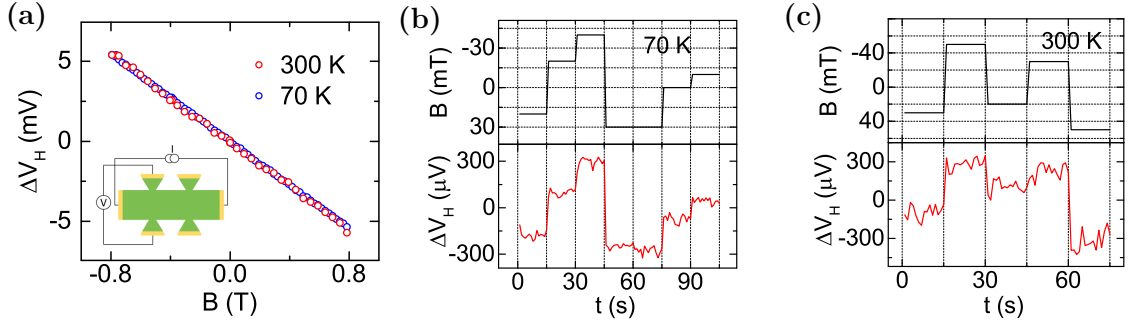


**Figure 5.5:** Characterization of graphene Hall elements operation at two different temperatures. (a) Output Hall voltage as a function of perpendicular magnetic field strength at 300 K and 70 K. Inset: measurement configuration. (b) Output Hall voltage as a function of time at different applied magnetic fields at 70 K and (c) 300 K. Measurements are shown at a bias current of  $90 \mu\text{A}$  and the background offset is subtracted from the data.

contacts  $V_1$ - $V_2$  or  $V_3$ - $V_4$ . From linear fitting according to equation 4.1 (taking into account background offset) the Hall mobilities were extracted using the relation  $\mu = 1/(e|n|R_s)$  [64] to be in the range of  $1000$ - $1700 \text{ cm}^2/\text{V s}^{-1}$  (Figure 5.4b) while carrier concentrations were in the range from  $7 \times 10^{12} \text{ cm}^{-2}$  to  $9 \times 10^{12} \text{ cm}^{-2}$  within the batch of 13 measured devices. The linearity error [15,23,28] in best samples was fluctuating at an average level of 2 % at 300 K down to 0.4 % at 70 K. Hall voltage responses measured as a function of time at different perpendicular magnetic fields are shown in Figure 5.5b and Figure 5.5c. An improvement of operation of Hall sensors can also be seen from comparison of Figure 5.5b and Figure 5.5c. Here, the Hall measurement was carried out for fixed periods of time at different applied perpendicular magnetic fields at constant current bias of  $90 \mu\text{A}$  at room temperature and 70 K. The magnetic field of  $\sim 30 \text{ mT}$  can be resolved from the noise at room temperature down to  $8 \text{ mT}$  at 70 K.

From the Hall measurements the current-related sensitivity was extracted and analyzed according to equation 4.2 and the voltage-related sensitivity according to  $S_V = \frac{1}{V} \frac{\partial V_H}{\partial B} \Big|_{V=\text{const}}$ . From Figure 5.6a one can conclude that current-normalized

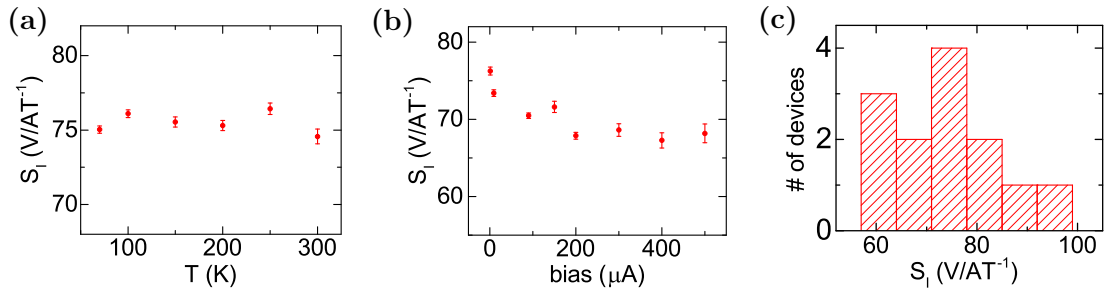


**Figure 5.6:** Current-related sensitivities ( $S_I$ ) of graphene Hall elements. (a) Temperature dependence of  $S_I$  at  $90 \mu\text{A}$  current bias. (b) Current bias dependence of  $S_I$  at room temperature. (c) Histogram of distribution of sensitivities  $S_I$  measured in 13 Hall elements at  $90 \mu\text{A}$  current bias and at room temperature.

sensitivities are thermally stable. The typical values are  $S_I \sim 75 \text{ V/AT}^{-1}$  for current-normalized and  $S_V \sim 0.007 \text{ V/VT}^{-1}$  for voltage-normalized sensitivities. The low  $S_V$  values could be attributed in particular to relatively high [38] contact and graphene resistances. The current bias dependence in Figure 5.6b shows slight decrease of  $S_I$  with applied bias. This decrease is due to increasing carrier concentration as current bias increases and could be caused by the drain-induced charge neutrality point shift [16,73,74]. The distribution of current-normalized sensitivities within the batch of 13 measured graphene Hall elements is depicted in Figure 5.6c with a maximum and minimum values  $97 \text{ V/AT}^{-1}$  and  $60 \text{ V/AT}^{-1}$  respectively.

The observed current-related sensitivities in large area all-CVD h-BN-encapsulated graphene devices are comparable to those in widely used magnetic Hall sensors based on Si. However, the graphene-based Hall sensors have additional advantages to be transparent and flexible. This work demonstrated the fabrication of h-BN/graphene/h-BN heterostructures-based Hall elements with 1D edge contacts prepared by using all-CVD materials available in the market. Such encapsulated heterostructures on large scale are promising for reliable and robust operation of graphene-based Hall sensors in different environmental conditions and commercial applications. These studies also open up the door to understanding the basic phenomenon that controls their performance. Optimizations of active region's dimensions and configuration can further enhance such Hall sensor performance. The device area was found to have a very significant impact on the operation of graphene magnetic Hall sensors, which could be related mainly to the quality of the heterostructures after the transfer process and increasing contribution of flicker noise to the observed signal [16,69]. The considered sensors would greatly benefit from the improved CVD growth methods of graphene/h-BN heterostructures and layer transfer techniques. The reduction of contacts resistance is also important for obtaining high voltage-related sensitivities. This could be achieved by optimization of fabrication process and, in particular, annealing the Hall sensor devices after fabrication of contacts as well as careful tuning of incorporation of interfacial species (such as oxygen e.g. during the etching process) at the 1D edge contact interface with graphene which could passivate graphene edge and increase current transmission [38].

### 5.3 Conclusions

In this chapter, the proof-of-concept for batch fabrication of Hall elements with h-BN-encapsulated graphene active region using only commercially available CVD materials is demonstrated for the first time. The graphene in investigated samples was connected via the 1D edge contacts with tunneling behavior, the presence of which could be attributed to the graphene termination chemistry and local oxidation of Ti in the contacts in proximity to the heterostructure edges. Hall measurements were performed on the studied batch-fabricated samples and time-dependent Hall response at different applied magnetic fields revealed minimum magnetic field resolution from the noise below  $30 \text{ mT}$  at room temperature. The current-related sensitivities within the batch of 13 studied samples were in the range of  $60\text{-}97 \text{ V/AT}^{-1}$  at room temperature. These demonstrations on large area all-CVD h-BN/graphene/h-

BN heterostructures bring graphene Hall sensors a big step closer to the market and have huge industrial relevance.



## Chapter 6

### Conclusions

The van der Waals heterostructures of 2D materials open a wide field of opportunities in electronics applications. In this thesis such heterostructures of graphene and hexagonal boron nitride were utilized in the active regions of investigated devices for such applications as Hall sensors and spin valves. While the graphene in these devices was used as a channel material due to its beneficial properties, the hexagonal boron nitride provided the necessary protection of atomically thin graphene sheet from environmental negative influences for reliable and durable operation. The 1D edge contacts to graphene sheet were exploited to mitigate the challenges and limitations introduced by conventional approach of graphene surface metallization for connecting the active region to the outputs.

The investigated devices were fabricated by means of electron or laser beam lithography and electron beam evaporation of metals. All heterostructures were prepared on only large area commercially available CVD graphene. Characterization by Raman spectroscopy and electrical transport measurements of prepared heterostructures revealed reliable material properties.

While aiming at the study of electrical spin injection into graphene channel through 1D ferromagnetic edge contacts and subsequent spin transport and detection, the operation of novel lateral spin valve devices utilizing heterostructures of CVD graphene protected by exfoliated h-BN was investigated by means of electrical measurements in nonlocal geometry. The observed behaviour of magnetoresistance switching while sweeping the in-plane external magnetic fields under different gate voltages allowed to rule out the spin-related nature of the observed signal and pointed to the influence of local Hall effects in the presence of fringe fields from ferromagnetic contacts. The measured temperature and bias dependencies were in accordance with this argument.

The fabricated graphene Hall elements with active regions consisting of CVD graphene/exfoliated h-BN heterostructures and connected to the outputs via the 1D edge contacts to graphene were investigated by means of Hall measurements. These sensors demonstrated magnetic field resolution at room temperature in the millitesla range and stable bias dependence of current-related sensitivity, which was found to reach up to  $366 \text{ V/AT}^{-1}$ .

However, the utilization of exfoliation method for preparation of heterostructures consisting of CVD graphene and flakes of h-BN, although it provides good material quality, limits the application potential of graphene Hall sensors. To advance

the fabrication technology of such sensors towards industry-compatible, large-scale manufacturing and approach the graphene-based Hall elements to commercialization, one step further was undertaken. Thus, a number of these devices were batch-fabricated on large area all-CVD heterostructures consisting of graphene sheet fully encapsulated in h-BN with the 1D edge contacts to the active regions. The electrical Hall measurements on these devices revealed the minimum magnetic field resolution from the noise below  $30\text{ mT}$  while current-related sensitivities within the batch of 13 measured devices were comparable to those of widely used Si-based Hall sensors and found to be in the range of  $60 - 97\text{ V/AT}^{-1}$  at room temperature.

These demonstrations lay basis for understanding and optimization of the phenomena that controls the operation of graphene nonlocal spin valve devices with 1D edge contacts and bring the technology of graphene Hall elements fabrication one step closer to commercialization.

## Appendix A

### Low-temperature operation of Hall sensors with exfoliated h-BN protection

The typical output Hall voltage response of graphene Hall element with exfoliated h-BN protection from the top at 70 K one can see on figure A.1a. The linearity error [15,23,28] fluctuates around the average level of 1.7 %. Figures A.1b and A.1c demonstrate gate tunability of Hall sensors' operation at 75 K. Changing the carrier concentration in graphene by sweeping the back gate voltage allowed to tune current-related sensitivity ( $S_I$ ) up to  $366 \text{ V}/\text{AT}^{-1}$ .

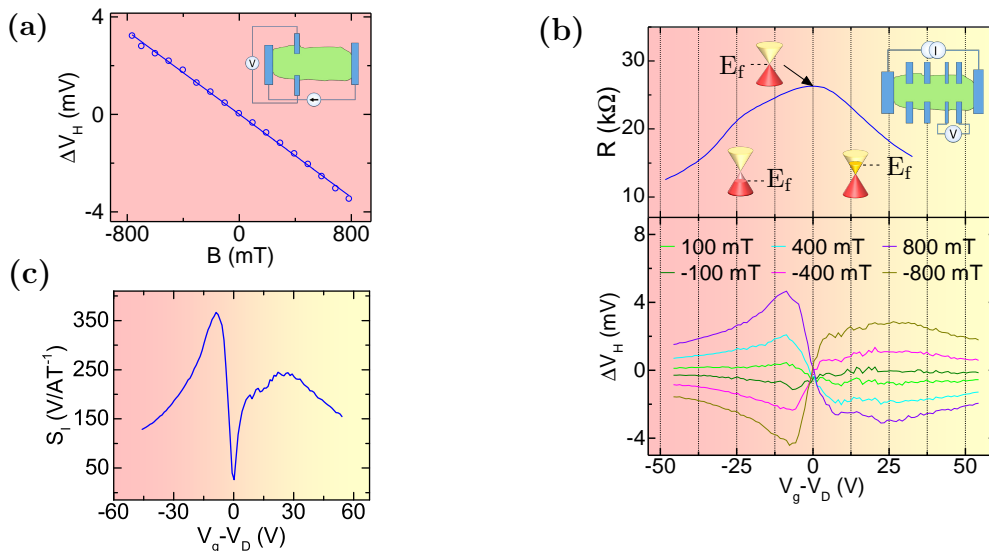


**Figure A.1:** Operation of graphene Hall sensors at low temperature. (a) Output Hall voltage as a function of perpendicular magnetic field strength at 70 K and zero gate voltage with subtracted background voltage offset (circles) along with linear fitting according to equation 4.1 (solid line). Inset: measurement configuration. (b) Back gate dependence of graphene resistance (top) and Hall voltage response as a function of back gate voltage at 75 K and at different perpendicular magnetic fields with subtracted response at 0 T of applied field (bottom). Measurement configuration for top panel is shown in the inset along with schematics of Dirac cones in graphene with positions of Fermi level at different regions of applied gate voltage. (c) Current-related sensitivity ( $S_I$ ), calculated from bottom panel of (b) as explained in section 4.2, as a function of gate voltage at 75 K. In all plots current bias is  $15 \mu\text{A}$ . Gradients of background color indicate the transition of graphene conduction from p-type (pink) to n-type (yellow). The horizontal axes are centered around the charge neutrality point in (b) and (c). Measurement configurations in bottom panel of (b) is the same as depicted in the inset of (a).



# Appendix B

## Recipes for sample fabrication

The processing steps followed during fabrication of devices investigated in Chapters 3 and 4 are listed in Section B.1, whereas processing steps for fabrication of devices investigated in Chapter 5 are listed in Section B.2.

### B.1 Devices fabricated on CVD graphene/exfoliated h-BN heterostructures

- Wafer-scale transfer of CVD graphene from copper substrate onto Si/SiO<sub>2</sub> substrate (service of Graphenea [41]).
- Anneal in Ar/H<sub>2</sub> (95 %/5 %) atmosphere at 500 °C for 45 min.
- Exfoliate hexagonal boron nitride flakes.
- Clean in warm (60 °C) acetone for 5 min followed by rinsing in IPA and blow-drying with N<sub>2</sub>.
- Oxygen plasma etch for 40 s under 50 W power to etch superfluous graphene.
- Spin-coat MMA EL8 copolymer at 6000 rpm for 1 min, bake at 135 °C for 10 min.
- Spin-coat ARP 6200.13 1:2 at 6000 rpm for 1 min, bake at 135 °C for 10 min.
- Expose with electron beam at 100 kV voltage and current 2 nA for small structures, 10 nA for bigger structures.
- Develop with n-amylacetat for 40 s.
- Directly transfer into MIBK:IPA 1:1 and keep for 75 s, blow-dry with N<sub>2</sub> without rinsing.
- Deposit 0.4 nm of Ti using electron beam evaporation at  $5 \times 10^{-7}$  Torr and oxidize it in pure oxygen atmosphere at 10 Torr for 10 min.
- Repeat previous step.
- Deposit 65 nm of Co at  $5 \times 10^{-7}$  Torr using electron beam evaporation.
- Liftoff the superfluous deposited materials along with the resist mask in warm (60 °C) acetone for 10 min, rinse in IPA and blow-dry with N<sub>2</sub>.

## B.2 Batch-fabricated Hall elements on all-CVD h-BN/graphene/h-BN heterostructures

- Wafer-scale transfer of all-CVD h-BN/graphene/h-BN materials from copper substrate onto Si/SiO<sub>2</sub> substrate (service of Graphenea [41]).
- Anneal in Ar/H<sub>2</sub> (95 %/5 %) atmosphere at 450 °C for 45 min.
- Spin-coat HMDS at 3000 rpm for 1 min.
- Spin-coat S1813 at 3000 rpm for 1 min, bake at 90 °C for 2 min.
- Expose with laser beam (DWL 2000 from Heidelberg Instruments tool used with diode 405 nm laser).
- Develop in MF319 for 40 s, rinse in H<sub>2</sub>O and blow-dry with N<sub>2</sub>.
- Using electron beam evaporation deposit thin film of 20 nm Al at  $5 \times 10^{-7}$  Torr.
- Liftoff the superfluous Al along with the resist mask in warm (60 °C) acetone for 10 min, rinse in IPA and blow-dry with N<sub>2</sub>.
- Etch the Al-unprotected regions of h-BN/graphene/h-BN heterostructures with plasma consisting of CHF<sub>3</sub> (40 sccm) and O<sub>2</sub> (4 sccm) at 50 mTorr and 50 W for 1 min.
- Etch away the Al hard mask in MF319, rinse in H<sub>2</sub>O and blow-dry with N<sub>2</sub>.
- Anneal in Ar/H<sub>2</sub> (95 %/5 %) atmosphere at 500 °C for 30 min.
- Spin-coat HMDS at 3000 rpm for 1 min.
- Spin-coat S1813 at 3000 rpm for 1 min, bake at 90 °C for 2 min.
- Expose with laser beam.
- Develop in MF319 for 40 s, rinse in H<sub>2</sub>O and blow-dry with N<sub>2</sub>.
- Expose to oxygen plasma at 25 W for 3 s.
- Using electron beam evaporation deposit 20 nm Ti followed by 60 nm Au at  $5 \times 10^{-7}$  Torr.
- Liftoff the superfluous deposited materials along with the resist mask in warm (60 °C) acetone for 10 min, rinse in IPA and blow-dry with N<sub>2</sub>.

## Bibliography

- [1] International Technology Roadmap for Semiconductors 2.0 (ITRS 2.0), 2015 Edition, <http://www.itrs2.net>
- [2] K.S. Novoselov, A.K. Geim, S.V. Morozov, D. Jiang, Y. Zhang, S.V. Dubonos, I.V. Grigorieva, A.A. Firsov, Electric field effect in atomically thin carbon films, *Science* **22**, 666 (2004).
- [3] A.K. Geim, I.V. Grigorieva, Van der Waals heterostructures, *Nature* **499**, 419–425 (2013).
- [4] Y. Liu, N.O. Weiss, Xidong Duan, H.-C. Cheng, Y. Huang and Xianfeng Duan, Van der Waals heterostructures and devices, *Nat. Rev. Mater.*, 16042 (2016).
- [5] K.S. Novoselov, A. Mishchenko, A. Carvalho and A.H. Castro Neto, 2D materials and van der Waals heterostructures, *Science* **353**, 461 (2016).
- [6] K.S. Novoselov, V.I. Fal’ko, L. Colombo, P.R. Gellert, M.G. Schwab and K. Kim, A roadmap for graphene, *Nature* **490**, 192–200 (2012).
- [7] A.C. Ferrari, F. Bonaccorso, V. Fal’ko, K.S. Novoselov, S. Roche, P. Bøggild, S. Borini, F.H.L. Koppens, V. Palermo, N. Pugno, J.A. Garrido, R. Sordan, A. Bianco, L. Ballerini, M. Prato, E. Lidorikis, J. Kivioja, C. Marinelli, T. Ryhänen, A. Morpurgo, J.N. Coleman, V. Nicolosi, L. Colombo, A. Fert, M. Garcia-Hernandez, A. Bachtold, G.F. Schneider, F. Guinea, C. Dekker, M. Barbone, Z. Sun, C. Galiotis, A.N. Grigorenko, G. Konstantatos, A. Kis, M. Katsnelson, L. Vandersypen, A. Loiseau, V. Morandi, D. Neumaier, E. Treossi, V. Pellegrini, M. Polini, A. Tredicucci, G.M. Williams, B.H. Hong, J.-H. Ahn, J.M. Kim, H. Zirath, B.J. van Wees, H. van der Zant, L. Occhipinti, A. Di Matteo, I.A. Kinloch, T. Seyller, E. Quesnel, X. Feng, K. Teo, N. Rupesinghe, P. Hakonen, S.R.T. Neil, Q. Tannock, T. Löfwander and J. Kinaret, Science and technology roadmap for graphene, related two-dimensional crystals, and hybrid systems, *Nanoscale* **7**, 4598–4810 (2015).
- [8] A.H. Castro Neto, F. Guinea, N.M.R. Peres, K.S. Novoselov and A.K. Geim, The electronic properties of graphene, *Rev. Mod. Phys.* **81**, 109 (2009).
- [9] T.O. Wehling, A.M. Black-Schaffer and A.V. Balatsky, Dirac materials, *Adv. Phys.* **63**, 1–76 (2014).
- [10] K.S. Novoselov, A.K. Geim, S.V. Morozov, D. Jiang, M.I. Katsnelson, I.V. Grigorieva, S.V. Dubonos, Two-dimensional gas of massless Dirac fermions in graphene, *Nature* **438**, 197–200 (2005).
- [11] I. Žutić, J. Fabian and S.D. Sarma, Spintronics: Fundamentals and applications, *Rev. Mod. Phys.* **76**, 323 (2004).
- [12] S. Roche, J. Åkerman, B. Beschoten, J.-C. Charlier, M. Chshiev, S.P. Dash, B. Dlubak, J. Fabian, A. Fert, M. Guimarães, F. Guinea, I. Grigorieva,

- C. Schönenberger, P. Seneor, C. Stampfer, S. O Valenzuela, X. Waintal and B. van Wees, Graphene spintronics: the European Flagship perspective, *2D Mater.* **2**, 030202 (2015).
- [13] W. Han, R.K. Kawakami, M. Gmitra and J. Fabian, Graphene spintronics, *Nat. Nanotechnol.* **9**, 794-807 (2014).
- [14] M.V. Kamalakar, C. Groenveld, A. Dankert and S.P. Dash, Long distance spin communication in chemical vapour deposited graphene, *Nat. Commun.* **6**, 6766 (2015).
- [15] H. Xu, Z. Zhang, R. Shi, H. Liu, Z. Wang, S. Wang, and L.-M. Peng, Batch-fabricated high-performance graphene Hall elements, *Sci. Rep.* **3**, 1207 (2013).
- [16] L. Huang, Z. Zhang, B. Chen, X. Ma, H. Zhong, and L.-M. Peng, Ultra-sensitive graphene Hall elements, *Appl. Phys. Lett.* **104**, 183106 (2014).
- [17] J. Dauber, A.A. Sagade, M. Oellers, K. Watanabe, T. Taniguchi, D. Neumaier, and C. Stampfer, Ultra-sensitive Hall sensors based on graphene encapsulated in hexagonal boron nitride, *Appl. Phys. Lett.* **106**, 193501 (2015).
- [18] T. Ciuk, O. Petruk, A. Kowalik, I. Jozwik, A. Rychter, J. Szmidski and W. Strupinski, Low-noise epitaxial graphene on SiC Hall effect element for commercial applications, *Appl. Phys. Lett.* **108**, 223504 (2016).
- [19] Z. Wang, M. Shaygan, M. Otto, D. Schall and D. Neumaier, Flexible Hall sensors based on graphene, *Nanoscale* **8**, 7683 (2016).
- [20] Z. Wang, L. Banszerus, M. Otto, K. Watanabe, T. Taniguchi, C. Stampfer and D. Neumaier, Encapsulated graphene-based Hall sensors on foil with increased sensitivity, *Phys. Status Solidi B*, 1-5 (2016).
- [21] J. Heremans, Solid state magnetic field sensors and applications, *J. Phys. D: Appl. Phys.* **26**, 1149-1168 (1993).
- [22] G. Boero, M. Demierre, P.-A. Besse and R.S. Popovic, Micro-Hall devices: performance, technologies and applications, *Sens. Actuators A* **106**, 314-320 (2003).
- [23] R.S. Popovic, Hall Effect Devices, Second Edition, Institute Physics Publishing, 2004.
- [24] Magnetic Field Sensors Market by Type, Technology, Applications, and Geography—Forecasts & Analysis to 2013–2020, Markets and Markets Report, September 2014.
- [25] Magnetic Sensors Market Analysis by Technology (Hall Effect Sensing, AMR, GMR), by Application (Automotive, Consumer Electronics, Industrial) and Segment Forecasts to 2022, Grand View Research, February 2016.
- [26] V.P. Kunets, W.T. Black, Y.I. Mazur, D. Guzun, G.J. Salamo, N. Goel, T.D. Mishima, D.A. Deen, S.Q. Murphy and M.B. Santos, Highly sensitive micro-Hall devices based on  $\text{Al}_{0.12}\text{In}_{0.88}\text{Sb}/\text{InSb}$  heterostructures, *J. Appl. Phys.* **98**, 014506 (2005).
- [27] M. Bando, T. Ohashi, M. Dede, R. Akram, A. Oral, S.Y. Park, I. Shibusaki, H. Handa and A. Sandhu, High sensitivity and multifunctional micro-Hall sensors fabricated using  $\text{InAlSb}/\text{InAsSb}/\text{InAlSb}$  heterostructures, *J. Appl. Phys.* **105**, 07E909 (2009).

- 
- [28] T. Hara, M. Mihara, N. Toyoda and M. Zama, Highly Linear GaAs Hall Devices Fabricated by Ion Implantation, *IEEE Trans. Electron Dev.* **ED-29**, 78-82 (1982).
- [29] K. Vervaeke, E. Simoen, G. Borghs, and V.V. Moshchalkov, Size dependence of microscopic Hall sensor detection limits, *Rev. Sci. Instrum.* **80**, 74701 (2009).
- [30] P. Kejik, G. Boero, M. Demierre, and R.S. Popovic, An integrated micro-Hall probe for scanning magnetic microscopy, *Sens. Actuators A* **129**, 212–215 (2006).
- [31] K. Watanabe, T. Taniguchi and H. Kanda, Direct-bandgap properties and evidence for ultraviolet lasing of hexagonal boron nitride crystal, *Nat. Mater.* **3**, 404-409 (2004).
- [32] G. Giovannetti, P.A. Khomyakov, G. Brocks, P.J. Kelly and J. van den Brink, Substrate-induced band gap in graphene on hexagonal boron nitride: Ab initio density functional calculations, *Phys. Rev. B* **76**, 073103 (2007).
- [33] C.R. Dean, A.F. Young, I. Meric, C. Lee, L. Wang, S. Sorgenfrei, K. Watanabe and T. Taniguchi, Boron nitride substrates for high-quality graphene electronics, *Nat. Nanotechnol.* **5**, 722 (2010).
- [34] S.P. Dash, S. Sharma, J.C. Le Breton, J. Peiro, H. Jaffrès, J.-M. George, A. Lemaître and R. Jansen, Spin precession and inverted Hanle effect in a semiconductor near a finite-roughness ferromagnetic interface, *Phys. Rev. B* **84**, 054410 (2011).
- [35] P.K. Muduli, J. Barzola-Quiquia, S. Dusari, A. Ballestar, F. Bern, W. Böhlmann and P. Esquinazi, Large local Hall effect in pin-hole dominated multigraphene spin-valves, *Nanotechnology* **24**, 015703 (2013).
- [36] G. Giovannetti, P.A. Khomyakov, G. Brocks, V.M. Karpan, J. van den Brink and P.J. Kelly, Doping graphene with metal contacts, *Phys. Rev. Lett.* **101**, 026803 (2008).
- [37] E.J.H. Lee, K. Balasubramanian, R.T. Weitz, M. Burghard and K. Kern, Contact and edge effects in graphene devices, *Nat. Nanotechnol.* **3**, 486-490 (2008).
- [38] L. Wang, I. Meric, P.Y. Huang, Q. Gao, H. Tran, T. Taniguchi, K. Watanabe, L.M. Campos, D.A. Muller, J. Guo, P. Kim, J. Hone, K.L. Shepard and C.R. Dean., One-Dimensional Electrical Contact to a Two-Dimensional Material, *Science* **342**, 614 (2013).
- [39] M. Stepanova, S. Dew, Nanofabrication: techniques and principles, Springer-Verlag/Wien, 2012.
- [40] Y.-C. Lin, C.-C. Lu, C.-H. Yeh, C. Jin, K. Suenaga and P.-W. Chiu, Graphene annealing: how clean can it be?, *Nano Lett.* **12**, 414-419 (2012).
- [41] "Graphenea Inc.". <http://www.graphenea.com>.
- [42] "Graphene Supermarket". <https://graphene-supermarket.com>.
- [43] A.Z. Elorza, A.C. Perez, B.A. Rodriguez and A.P. Rodriguez, Method of manufacturing a graphene monolayer on insulating substrates, U.S. Patent: 20140001152 A1, issued date January 2, 2014.
- [44] A. Fert, Nobel Lecture: Origin, development, and future of spintronics, *Rev. Mod. Phys.* **80**, 1517 (2008).
- [45] J. Sinova and I. Žutić, New moves of the spintronics tango, *Nat. Mater.* **11**, 368–371 (2012).

- [46] S.P. Dash, S. Sharma, R.S. Patel, M.P. de Jong and R. Jansen, Electrical creation of spin polarization in silicon at room temperature, *Nature* **462**, 491-494 (2009).
- [47] A. Avsar, J.Y. Tan, T. Taychatanapat, J. Balakrishnan, G.K.W. Koon, Y. Yeo, J. Lahiri, A. Carvalho, A.S. Rodin, E.C.T. O'Farrell, G. Eda, A.H. Castro Neto and B. Özyilmaz, Spin-orbit proximity effect in graphene, *Nat. Commun.* **5**, 4875 (2014).
- [48] M.V. Kamalakar, A. Dankert, J. Bergsten, T. Ive and S.P. Dash, Enhanced Tunnel Spin Injection into Graphene using Chemical Vapor Deposited Hexagonal Boron Nitride, *Sci. Rep.* **4**, 6146 (2014).
- [49] N. Tombros, C. Jozsa, M. Popinciuc, H.T. Jonkman and B.J. van Wees, Electronic spin transport and spin precession in single graphene layers at room temperature, *Nature* **448**, 571-574 (2007).
- [50] G. Schmidt, D. Ferrand and L.W. Molenkamp, Fundamental obstacle for electrical spin injection from a ferromagnetic metal into a diffusive semiconductor, *Phys. Rev. B* **62**, R4790-R4793 (2000).
- [51] E.I. Rashba, Theory of electrical spin injection: Tunnel contacts as a solution of the conductivity mismatch problem, *Phys. Rev. B* **62**, R16267-R16270 (2000).
- [52] A. Fert and H. Jaffrès, Conditions for efficient spin injection from a ferromagnetic metal into a semiconductor, *Phys. Rev. B* **64**, 184420 (2001).
- [53] B. Dlubak, M.-B. Martin, C. Deranlot, B. Servet, S. Xavier, R. Mattana, M. Sprinkle, C. Berger, W.A. De Heer, F. Petroff, A. Anane, P. Seneor and A. Fert, Highly efficient spin transport in epitaxial graphene on SiC, *Nat. Phys.* **8**, 557-561 (2012).
- [54] W. Han, K. Pi, K.M. McCreary, Y. Li, J.J.I. Wong, A.G. Swartz and R.K. Kawakami, Tunneling Spin Injection into Single Layer Graphene, *Phys. Rev. Lett.* **105**, 167202 (2010).
- [55] L. Britnell, R.V. Gorbachev, R. Jalil, B.D. Belle, F. Schedin, M.I. Katsnelson, L. Eaves, S.V. Morozov, A.S. Mayorov, N.M.R. Peres, A.H. Castro Neto, J. Leist, A.K. Geim, L.A. Ponomarenko and K.S. Novoselov, Electron Tunneling through Ultrathin Boron Nitride Crystalline Barriers, *Nano Lett.* **12**, 1707-1710 (2012).
- [56] A.C. Ferrari, J.C. Meyer, V. Scardaci, C. Casiraghi, M. Lazzeri, F. Mauri, S. Piscanec, D. Jiang, K.S. Novoselov, S. Roth and A.K. Geim, Raman spectrum of graphene and graphene layers, *Phys. Rev. Lett.* **97**, 187401 (2006).
- [57] R.V. Gorbachev, I. Riaz, R.R. Nair, R. Jalil, L. Britnell, B.D. Belle, E.W. Hill, K.S. Novoselov, K. Watanabe, T. Taniguchi, A.K. Geim, P. Blake, Hunting for Monolayer Boron Nitride: Optical and Raman Signatures, *Small* **7**, 465-468 (2011).
- [58] M. Johnson and R.H. Silsbee, Calculation of nonlocal baseline resistance in a quasi-one-dimensional wire, *Phys. Rev. B* **76**, 153107 (2007).
- [59] M.V. Kamalakar, A. Dankert, J. Bergsten, T. Ive and S.P. Dash., Enhanced tunnel spin injection into graphene using chemical vapor deposited hexagonal boron nitride, *Sci. Rep.* **4**, 6146 (2014).

- 
- [60] F.G. Monzon, M. Johnson and L. Roukes, Strong Hall voltage modulation in hybrid ferromagnet/semiconductor microstructures, *Appl. Phys. Lett.* **71**, 3087-3089 (1997).
- [61] F.G. Monzon, D.S. Patterson, M.L. Roukes, Characterization of individual nanomagnets by the local Hall effect, *J. Magn. Magn. Mater.* **195**, 19-25 (1999).
- [62] M. Hara, A. Endo, S. Katsumoto, Y. Iye, Transport in ferromagnet/semiconductor 2DEG hybrid network structure, *Physica E* **22**, 345-348 (2004).
- [63] F.G. Monzon, H.X. Tang and M.L. Roukes, Magnetoelectronic Phenomena at a Ferromagnet-Semiconductor Interface, *Phys. Rev. Lett.* **84**, 5022 (2000).
- [64] N. Lindvall, Towards graphene-based devices: Fabrication and characterization, Thesis for the degree of licentiate of engineering, Chalmers University of Technology, 2012.
- [65] T. Fang, A. Konar, H. Xing and D. Jena, Carrier statistics and quantum capacitance of graphene sheets and ribbons, *Appl. Phys. Lett.* **91**, 092109 (2007).
- [66] T. Maassen, F.K. Dejene, M.H.D. Guimarães, C. Józsa and B.J. van Wees, Comparison between charge and spin transport in few-layer graphene, *Phys. Rev. B* **83**, 115410 (2011).
- [67] M. Diaz-Michelena, Small magnetic sensors for space applications, *Sensors* **9**, 2271-2288 (2009).
- [68] E. Ramsden, Hall-effect sensors: theory and applications, Second edition, Elsevier Inc., 2006.
- [69] H. Xu, L. Huang, Z. Zhang, B. Chen, H. Zhong and L.-M. Peng, Flicker noise and magnetic resolution of graphene hall sensors at low frequency, *Appl. Phys. Lett.* **103**, 112405 (2013).
- [70] J. Park, S.B. Jo, Y.-J. Yu, Y. Kim, J.-W. Yang, W.H. Lee, H.H. Kim, B.H. Hong, P. Kim, K. Cho and K.S. Kim, Single-gate bandgap opening of bilayer graphene by dual molecular doping, *Adv. Mater.* **24**, 407-411 (2012).
- [71] D.R. Lenski and M.S. Fuhrer, Raman and optical characterization of multilayer turbostratic graphene grown via chemical vapor deposition, *J. Appl. Phys.* **110**, 013720 (2011).
- [72] B.J. Jönsson-Åkerman, R. Escudero, C. Leighton, S. Kim and I.K. Schuller, Reliability of normal-state current-voltage characteristics as an indicator of tunnel-junction barrier quality, *Appl. Phys. Lett.* **77**, 1870 (2000).
- [73] S.A. Thiele, J.A. Schaefer and F. Schwierz, Modeling of graphene metal-oxide-semiconductor field-effect transistors with gapless large-area graphene channels, *J. Appl. Phys.* **107**, 094505 (2010).
- [74] J. Bai, L. Liao, H. Zhou, R. Cheng, L. Liu, Y. Huang and D. Duan, Top-Gated Chemical Vapor Deposition Grown Graphene Transistors with Current Saturation, *Nano Lett.* **11**, 2555 (2011).